Spring 2024

GRAPHENE REINFORCED POLYMER COMPOSITE FOR SMALL-SCALE VERTICAL AXIS WIND TURBINE ROTORS

Kunal A. Bachim
University of Texas at Arlington

GRAPHENE REINFORCED POLYMER COMPOSITE FOR SMALL-SCALE VERTICAL AXIS WIND TURBINE ROTORS

by

KUNAL ANANT BACHIM

THESIS

Submitted in partial fulfillment of the requirements
for the degree of Master of Science in Aerospace Engineering at
The University of Texas at Arlington
May, 2024

Arlington, Texas

Supervising Committee:

Michael Bozlar, Supervising Professor
Catherine Kilmain
Sunand Santhanagopalan

ABSTRACT

GRAPHENE REINFORCED POLYMER COMPOSITE FOR SMALL-SCALE VERTICAL AXIS WIND TURBINE ROTORS

Kunal Anant Bachim , M.S.

The University of Texas at Arlington, 2024

Supervising Professor: Michael Bozlar

Polymers have evolved as an indispensable asset in various sectors ranging from packaging and construction to energy and aerospace. However, the accumulation of polymer waste poses a necessity to shift toward sustainable waste management processes. Mechanical recycling is a primary method in establishing a circular economy approach for polymers. However, a fundamental challenge arises in this process: a decrease in the mechanical performance of the recycled product compared to that of its pristine counterpart.

This project addresses the challenge of enhancing the recyclability of polyethylene terephthalate (PET) from discarded polymer material by incorporating graphene nanoparticles into the polymer matrix during the recycling stage. This elevates its mechanical performance and extends polymer material's recyclability. The discarded polymer was processed, reinforced with graphene oxide, and extruded into filaments using a twin-screw extruder. Several recycling rounds were conducted, and changes in the mechanical and chemical characteristics of the reinforced polymers were assessed.

The novel material is then inspected for its viability as a robust material for small-scale rotor turbine blades. Wind climate of a remote region in Sudan was assessed for its potential for harnessing wind energy by designing and analyzing a sustainable, small scale,

vertical-axis wind turbine rotor. The rotor undergoes modeling, aerodynamic simulation and structural analysis to evaluate its performance under the loading conditions generated by average and peak wind speeds in the remote region of Sudan.

DECLARATION OF ORIGINALITY

I, Kunal Anant Bachim, hereby declare that this master's thesis entitled "GRAPHENE REINFORCED POLYMER COMPOSITE FOR SMALL-SCALE VERTICAL AXIS WIND TURBINE ROTORS" is entirely my own work, based on my own research, study, and analysis. Any ideas, techniques, quotations from the work of other people are fully acknowledged. All the sources used in this thesis have been cited accurately in accordance with standard referencing practices.

Throughout the process of conducting research and writing this thesis, I have upheld the principles of academic integrity and honesty. I have not plagiarized the work of others nor have I used any unauthorized assistance in completing this thesis.

Furthermore, I declare that this is the true copy of my thesis, including any final revisions as approved by my supervising professor and has not been submitted in part or in full for any other degree or qualification at University of Texas at Arlington or any other Institution.

I understand the consequences of academic dishonesty, including but not limited to the revocation of my degree, and I affirm that the work presented in this thesis is original, authentic, and represents my own intellectual efforts.

ACKNOWLEDGEMENT

I am indebted to my supervising professor, Dr. Michael Bozlar, for providing me with a place to work, invaluable research opportunities, guidance, and insights in the areas of polymer science and engineering throughout my tenure at the University of Texas at Arlington. Your expertise and belief in my research have been instrumental in shaping this thesis.

I would also like to thank the members of my thesis committee whose constructive feedback has enriched the depth and quality of this thesis. I am grateful for their dedication to excellence and their willingness to share their knowledge and expertise generously.

Additionally, I would like to extend my appreciation to the faculty and staff of the Mechanical and Aerospace Engineering department, whose resources and assistance have facilitated the completion of this thesis.

Lastly, I would like to thank all the individuals whose contributions, whether direct or indirect, have played a part in the completion of this thesis. Your support has been valuable in shaping my academic and personal growth.

DEDICATION

This thesis is dedicated to my parents, Swati Bachim and Anant Bachim, whose unwavering support and encouragement have been the cornerstone of my academic journey. Your sacrifices and guidance have shaped me into the person I am today, and I am forever grateful for your belief in me.

To my older brother, Abhishek, your counsel, and constant motivation have been invaluable to me throughout this endeavor. Your belief in my abilities has fueled my determination to reach this milestone.

I also extend my heartfelt appreciation to all my friends whose support has been a constant reminder of the power of friendship, and I am grateful for the joy and inspiration you have brought into my life.

Thank you for always being my pillars of strength and for believing in my dreams.

TABLE OF CONTENTS

LIST OF FIGURES

LIST OF TABLES

LIST OF SYMBOLS

Symbol	SI Unit	Description
α	-	Airfoil angle of attack
θ	-	Azimuth angle of blade
σ	-	Solidity factor
ω	rad/s	Angular velocity
C	m	Blade chord length
C_d	-	Coefficient of drag
C_l	-	Coefficient of lift
C_n	-	Normal force coefficient
C_p	-	Coefficient of performance
C_t	-	Tangential force coefficient
D	m	Diameter of rotor
F_n	N	Normal load
F_t	N	Tangential load
F_{tan}	N	Average tangential force
H	m	Rotor height
L	m	Lift force
M	kg	Mass
N	-	Number of blades
P	W	Power captured by turbine
P_w	W	Total power available in the wind
R	m	Rotor radius
T	Nm	Torque

Symbol	SI Unit	Description
u	-	Upstream interference factor
$u\prime$	-	Downstream interference factor
V_c	m/s	Chordal component of velocity
V_e	m/s	Equilibrium velocity
V_i	m/s	Induced velocity
V_{iu}	m/s	Upstream induced velocity
V_{id}	m/s	Downstream induced velocity
V_n	m/s	Normal component of velocity
V_r	m/s	Relative velocity
V_∞	m/s	Free stream velocity

CHAPTER 1

INTRODUCTION

1.1 Polymer waste

Polymers are widely used materials in various sectors due to their versatility and affordability. However, disposing of waste polymer poses significant environmental challenges globally. The material's resilience to deterioration and its gradual degradation rates originate mainly from the molecular structures and chemical compositions of polymer chains. While these properties are highly advantageous during product use, they also present environmental challenges at the end of the product cycle.

Polymer waste can encompass a wide range of materials, including thermopolymers such as polycarbonates (PC), thermosets such as epoxy resins, elastomers like Ethylene-propylene-diene monomer rubber (EPDM), and fibers such as nylon.

Improper disposal of polymer waste can lead to pollution of land, water bodies, and air, harming ecosystems and wildlife. Over time, polymer waste can break down into smaller fragments, called micropolymers, which can accumulate in the environment and pose significant risks to aquatic organisms, terrestrial animals, and humans. The production, disposal, and combustion of polymer materials can contribute to greenhouse gas emissions, worsening the impact on the climate.

Effective management and recycling of polymer waste is essential to minimize its environmental impact and promote a circular economy for polymers. some of the present strategies to help manage the waste are reducing the use of single-use polymers, advanced recycling technologies, waste-to-energy processes and disposal of polymer waste in landfills.

1.2 Polyethylene terephthalate

Polyethylene terephthalate (PET) is one of the most widely used polymers with a low recycling rating which denotes that it loses its mechanical properties when it undergoes mechanical recycling. Its structure is formed through the reaction of two monomers: ethylene glycol and terephthalic acid (or dimethyl terephthalate).

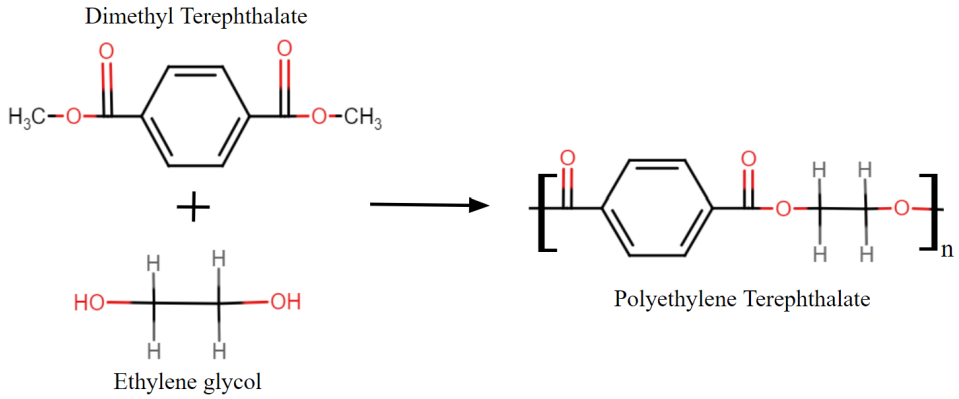

Figure 1.1: Formation of Polyethylene Terephthalate

The synthesis of PET involves a condensation polymerization reaction between these monomers, resulting in the formation of long chains of repeating units. In this process, the hydroxyl (-OH) groups of ethylene glycol react with the carboxyl (-COOH) groups of terephthalic acid (or dimethyl terephthalate) in the presence of a catalyst, typically antimony trioxide. This reaction leads to the formation of ester bonds (-COO-) between the monomers, which is used to link them together to form the polymer chain.

1.3 Methods of recycling

Polymer recycling employs two primary methods: mechanical and chemical. Mechanical recycling involves physically processing polymers to create new products, while chemical recycling breaks down polymers into their molecular components for reuse in manufacturing.

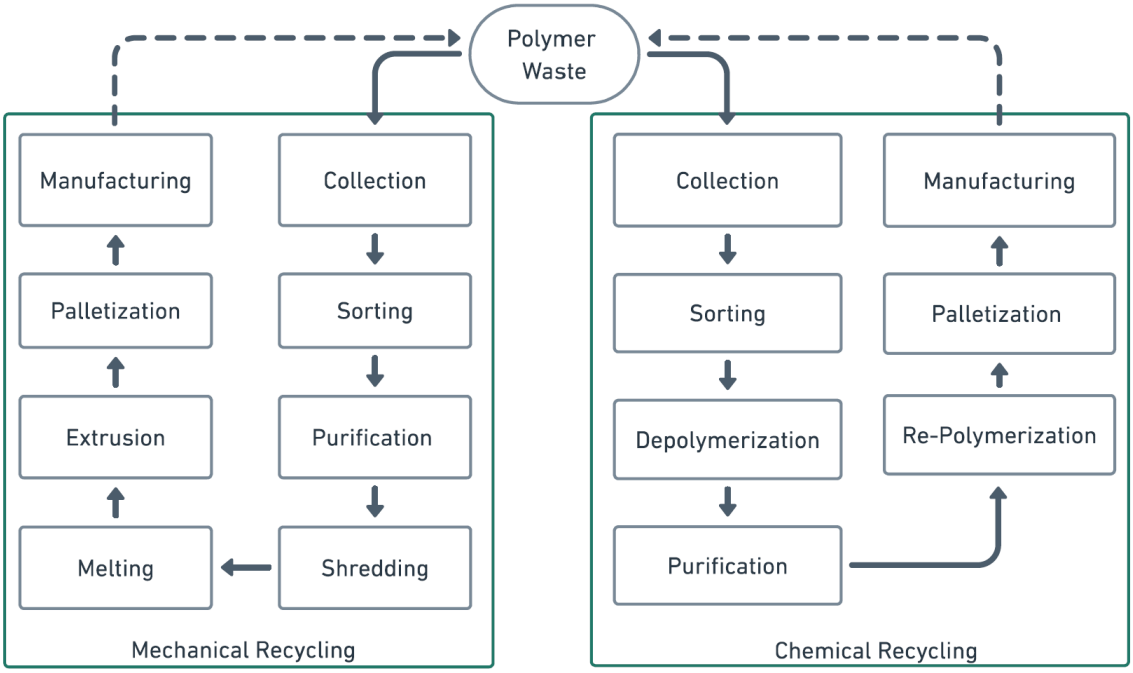

Figure 1.2: Chemical and mechanical recycling processes

1.3.1 Chemical recycling

Chemical recycling, also known as advanced recycling, offers the potential to break down polymers into their original monomers, essentially allowing the creation of new polymers with properties similar to those of pristine materials. Unlike mechanical recycling, which involves physical processes, chemical recycling uses chemical reactions. This process can yield polymers which are chemically similar to those that were first synthesized. Such processes have the capacity to recycle a wide range of polymers, including those difficult to recycle through mechanical means, and can renew their useful life. Chemical recycling processes often require specialized equipment and controlled environments to ensure the desired chemical reactions occur safely. Some processes produce toxic byproducts or emissions, which need to be carefully managed to minimize environmental and health risks.

1.3.2 Mechanical recycling

Mechanical recycling is the most widely used industrial process used to convert polymer waste into new products through physical methods rather than chemical reactions. Waste is collected from various sources, including households, businesses, and industries. The bulk collected is then sorted on the basis of polymer type. Automated sorting systems, as well as manual sorting by trained workers, are often used for this purpose.

Once sorted, the polymer waste undergoes cleaning and pre-processing to remove contaminants such as dirt, labels, adhesives, and food residues etc. This cleaning process is crucial to ensure the quality of the recycled polymer material.

The cleaned polymer waste is then mechanically shredded or granulated into smaller pieces or flakes. Shredding increases the surface area of the polymer, making it easier to handle and process in subsequent steps.

The extruded polymer strands are then cooled and cut into small pellets or granules using pelletizing equipment. Pelletization helps standardize the size and shape of recycled polymer material, making it easier to handle, transport, and use in manufacturing processes. Recycled polymer pellets are finally used as raw material in the manufacture of new polymer products.

1.4 Graphene reinforced polymers

Graphene is a two-dimensional carbon allotrope of carbon arranged in a honeycomb lattice, which has remarkable properties compared to other materials known to science. It has acquired significant interest across various scientific disciplines. In polymer science, the incorporation of graphene has led to notable advancements by dispersing graphene within polymer matrices. The resulting composite materials have been studied and have shown enhanced mechanical strength, electrical conductivity, and thermal conductivity [2].

Pure graphene, in its most pristine state, exhibits remarkable stability in its composi-

tion and demonstrates limited interaction with molecules from other materials. In contrast, graphene oxide features oxygenated groups containing (-o-) and (-OH) bonds, enhancing its capacity to engage with external molecules[3].

These graphene-polymer composites have applications in various fields, including aerospace, automotive, electronics, and biomedical engineering. The combination of graphene's unique properties with the versatile nature of polymers has opened numerous opportunities for the development of novel materials with controllable functionalities. In this study, a graphene reinforced polymer is studied in order to replace conventional aluminum rotor blade frames.

1.5 Vertical axis wind turbines

In the vertical axis wind turbines, as the name suggests, the turbine's axis of rotation is aligned vertically and the wind velocity vector is perpendicular to this axis. The blades of the rotor revolve when the wind is encountered, this attached to a generator shaft generates electrical energy. various types of VAWTs are discussed further.

Traditionally, VAWTs are manufactured with aluminum metal blades because of it's ease of availability and strength-to-weight ratio of the material. Small-scale turbine rotors represent a promising direct application for the novel material discussed in this work, offering distinct benefits, especially in terms of reduction in carbon footprint compared to traditional metal-blade VAWTs and the construction of a truly renewable wind energy generator.

VAWTs offers two key advantages: firstly, their omni-directional capability allows them to initiate rotation at low wind speeds and energy generation irrespective of wind direction. second, the size and scale of the turbine rotor makes them easy to either replace or repair and maintain, making them the most cost effective and simple technology to operate.

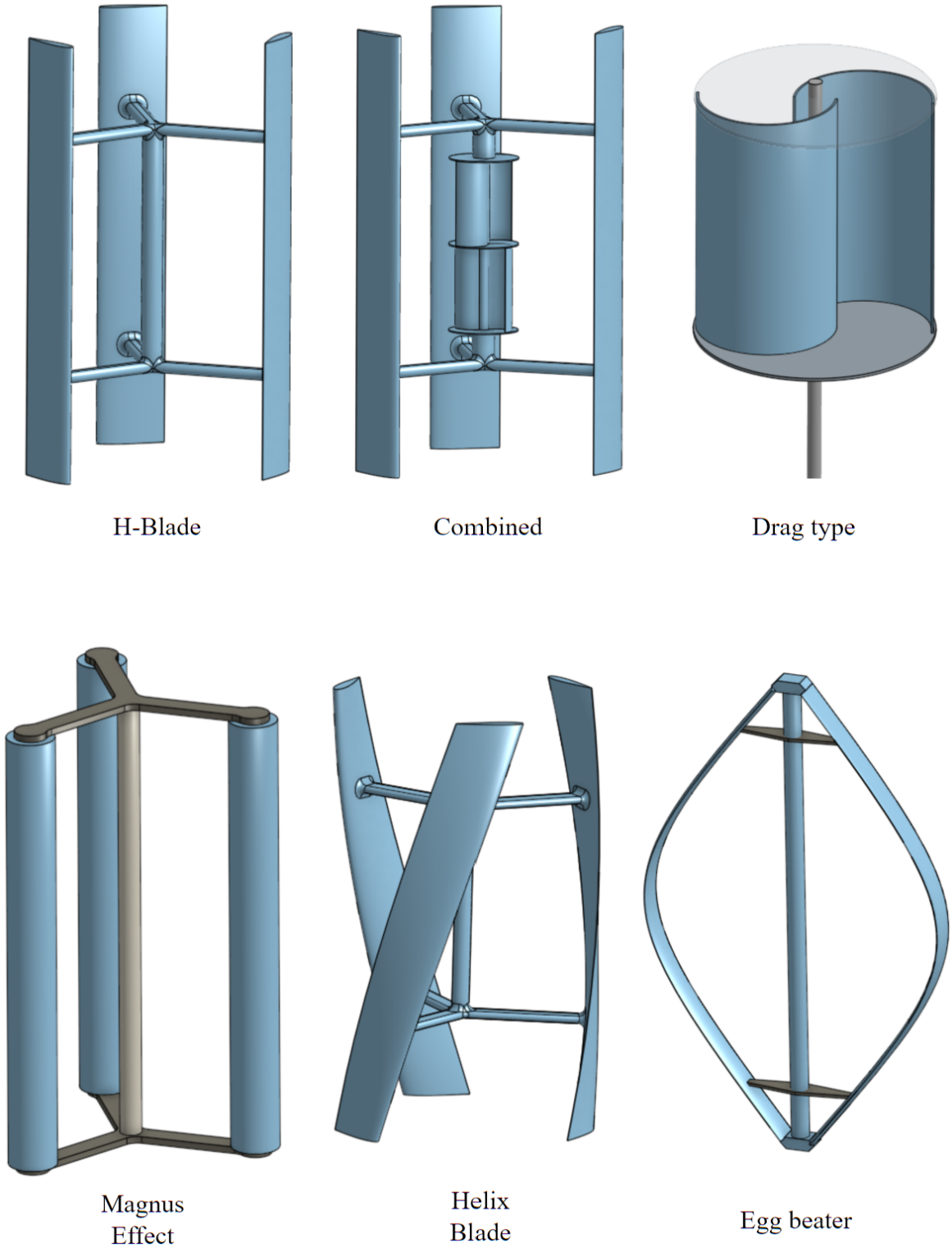

Figure 1.3: Types of vertical axis wind turbine

1.5.1 VAWT types

H-Blade

A commonly encountered variant of VAWT is the H-blade configuration, characterized by straight blades connected to a central shaft via horizontal struts, forming a shape reminiscent of the letter H. Its straightforward design makes it relatively easy to fabricate. In conditions of consistent wind flow, as the turbine rotates, each blade experiences a uniform distribution of lift and drag forces along its length. However, certain azimuthal angles are notable for producing maximum normal and tangential forces on the H-rotor blades, while others dictate distinct lift and drag profiles along their spans. This disparity in forces results in an overall imbalance, and a cycling loading from maximum to minimum force conditions, potentially inducing vibrations in the operational turbine. The size of the turbine is severely limited due to centrifugal force being generated during rotation which is discussed more in this work.

Drag type

A type of wind turbine known as a drag turbine or 'Savonius' type harnesses the kinetic energy of the wind by obstructing its flow. Typically, these turbines feature a semicircular cup design aimed at capturing the wind and translating its force into rotational motion. Rotation occurs when wind force exceeds the turbine's rotational inertia and initiates the torque required to start the generator shaft. Wind direction plays a crucial role, as there exists an optimal position for maximum wind capture. As the cups rotate, they face the wind from the side opposite where it initially impacts, allowing the wind to slip over the outward-curving shape. To ensure effective operation, the drag generated by the outward curve must be outweighed by the inward curve shape that captures the wind. The large surface area exposed to the wind and resulting drag on the return cycle of semicircular cup limits the efficiency of such turbines in rotation.

Combined type

Another innovative approach involves the integration of lift and drag turbine designs. Here, the drag turbine is positioned centrally, while the lift-type blades are located away from the center. The drag turbines are staggered atop one another, forming a semicircular shape rotated 90 degrees to capture wind from multiple directions. This combination enables the initiation of rotation at lower wind speeds. Once a specific rotational speed is attained, the lift-type blades assume the role of generating force, leveraging the torque induced by the lift vector. However, a significant tradeoff arises: As the lift-type blades take over, the centrally positioned drag turbine also rotates, producing drag that opposes the rotation. While this drag is generally minor, it's not negligible. Nonetheless, the combined effect facilitates turbine rotation at lower wind speeds.

Helical blade type

A clever solution to counteract a common issue with straight-bladed turbine rotors involves the adoption of helical-shaped blades. Unlike their straight counterparts, helical blade turbine blades generate distributed lift, drag, and resulting tangential force along their spans. This alteration significantly reduces torque oscillations, leading to smoother force profiles across the blade's azimuthal locations [4]. The influence of centrifugal force on its helical shape results in the blade experiencing outward normal forces distributed along the blade span. Consequently, the blade undergoes torsion in addition to bending. While the overall efficiency of such helical-shaped rotor blades is advantageous due to the production of continuous torque spread across azimuthal angles, these rotors require higher wind speeds to initiate rotation initially.

Magnus effect turbine

The Magnus effect, a phenomenon in which a spinning object encounters a force perpendicular to its direction of travel [5], has found application in various industries. Turbines leveraging this effect have been devised for specific regions with exceptionally high wind speeds or for harnessing energy from tornadoes and cyclones. Typically, a small straight flap is positioned in close proximity to the turbine's cylindrical rotating components to guide airflow and generate tangential force. However, freely rotating cylinders fail to sustain continuous rotation of turbine, as the cylindrical elements tend to rotate in opposing directions based on their azimuthal position and the wind's direction. To address this, a control mechanism is employed to regulate the cylinder's rotation, thereby maintaining its spin direction. A significant advantage of this modification is the ability to control the cylinder rotation speeds even in extreme wind conditions. Consequently, the turbine becomes viable and safe for operation during hurricanes, as rotor RPM can be managed to extract energy from high-speed winds.

Egg-beater rotor

In an attempt to mitigate the impact of centrifugal force on turbine blades, engineers have developed the egg beater turbine, aptly named due to its resemblance to an egg beater in shape. This turbine features blades whose starting and ending sections are closer to the axis of rotation, with the central portion extending outward [6]. This distribution of mass around the rotating axis significantly reduces centrifugal force, allowing for the construction of larger Vertical Axis Wind Turbines (VAWTs) compared to other designs. Additionally, this blade configuration maximizes torque production at the sections farthest from the center, with torque diminishing as distance from the central axis decreases. The angles of the blades relative to the vertical axis also play a crucial role in generating tangential force and must be

carefully considered when assessing performance. During rotation, the mass situated away from the center exerts tension on the blade elements, contributing to their overall dynamics.

1.6 Site selection and wind climate analysis

Determining the location of a horizontal axis wind turbine (HAWT) involves understanding the predominant wind direction. On the other hand, Vertical Axis Wind Turbines (VAWTs) can rotate independently of wind direction. Nonetheless, HAWTs, being larger, typically harness winds at higher altitudes where speeds are generally greater than at ground level. whereas small-scale VAWTs, due to their smaller size, lack access to higher altitudes, making regions with high surface wind speeds more favorable for their deployment.

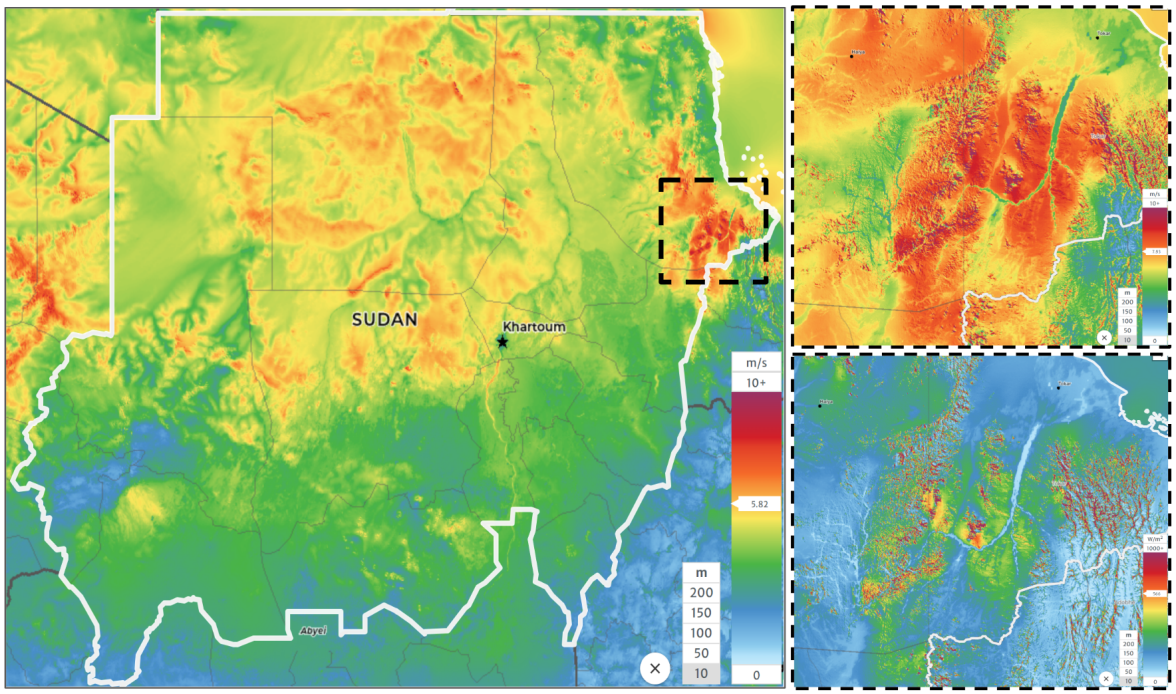

Figure 1.4: East Sudan, distribution of wind speed and mean power density

Sudan, situated on the African continent, has faced numerous hurdles in meeting its energy needs, leading to an ongoing energy crisis [7]. The eastern region of Sudan is particularly interesting because of its considerable potential for harnessing wind energy. This area

is under consideration for further study in this work. Across the entirety of Sudan, the average wind speed over the landscape at approximately 6 meters per second [8]. However, the region under examination stands out with notably heightened wind velocities. Specifically, in the mountainous terrain of eastern Sudan, the dynamics of the wind reveal an average speed of 7.84 meters per second, and certain areas experience even stronger gusts reaching up to 9.96 meters per second.

The mean power density is an important parameter considered for wind energy harvesting. It refers to the average amount of power available per unit area at a specific location. Figure 1.4 shows the wind speed gradient and the power density gradient in Sudan. In the eastern part of Sudan, the analysis reveals a range of mean power densities depicted in 1.5. The lowest recorded value stands at approximately 400 W/m², while the highest reaches up to 1500 W/m², with an average value of 880 W/m² [1]. This substantial wind energy potential in the mountainous regions of the east offers an attractive opportunity to investigate wind energy harvesting projects.

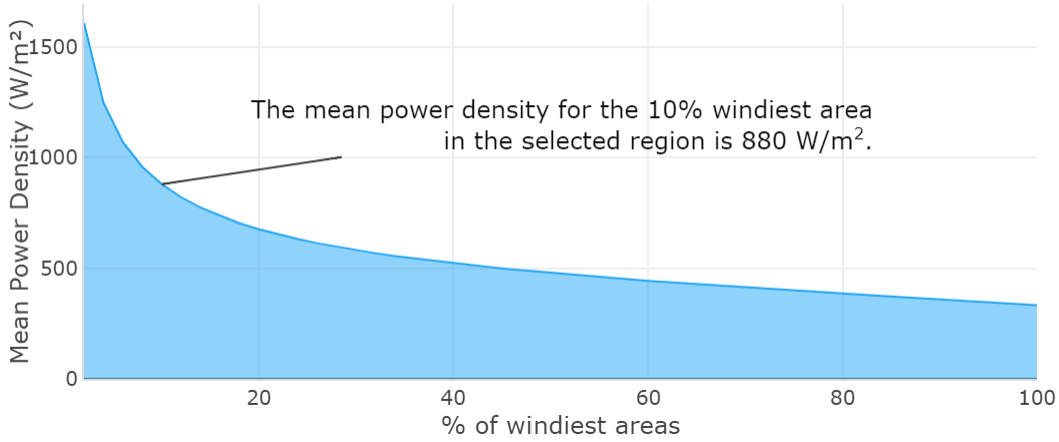

Figure 1.5: Mean power density, East Sudan

[1]Information obtained from the Global Wind Atlas version 3.3, a free, web-based application developed, owned and operated by the Technical University of Denmark (DTU). The Global Wind Atlas version 3.3 is released in partnership with the World Bank Group, using data provided by Vortex, using funding provided by the Energy Sector Management Assistance Program (ESMAP). For additional information: https://globalwindatlas.info

CHAPTER 2

METHODOLOGY

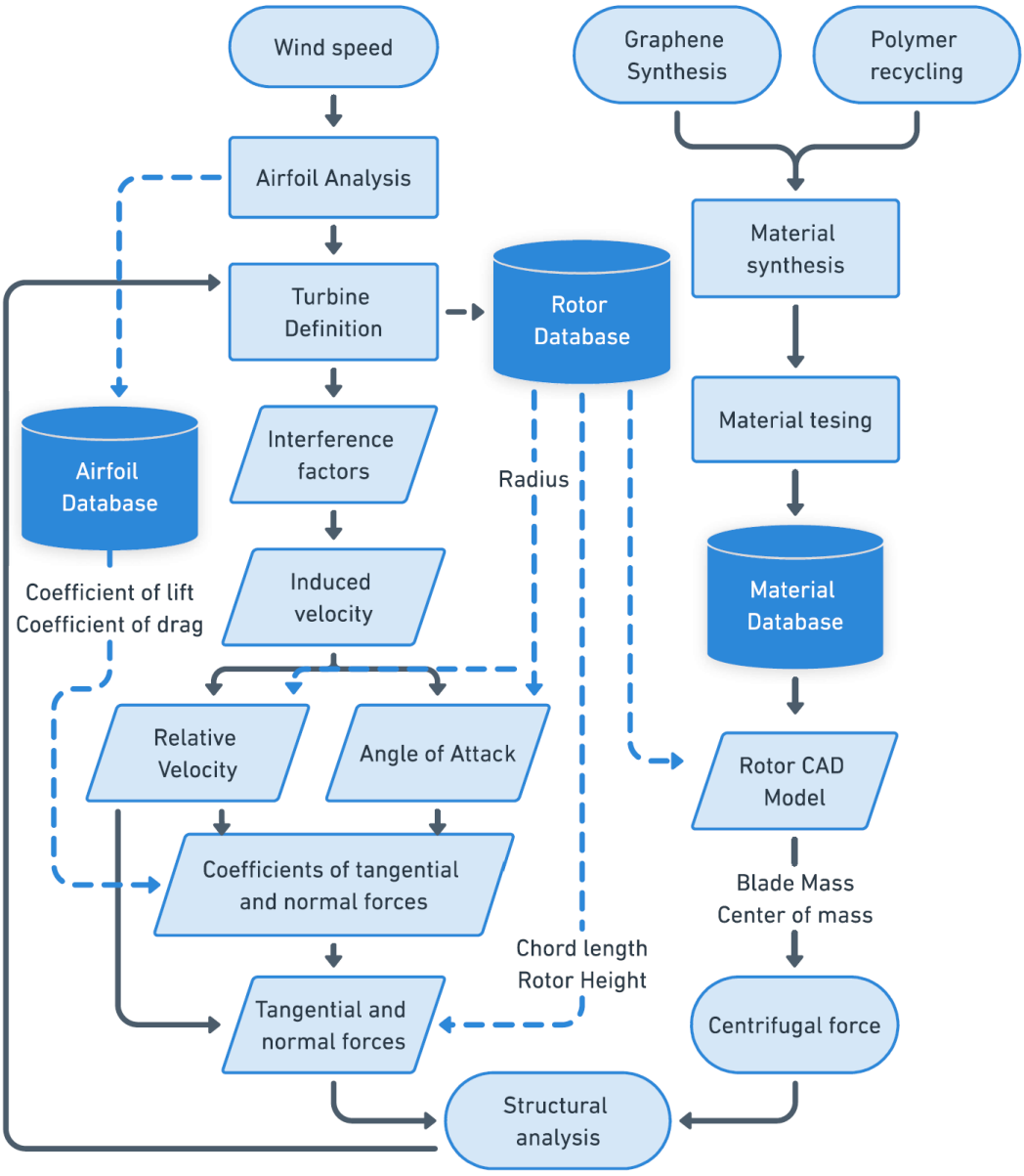

Figure 2.1: Novel polymer turbine-rotor design and analysis workflow[1]

2.1 Toolbox

2.1.1 DMST mathematical model

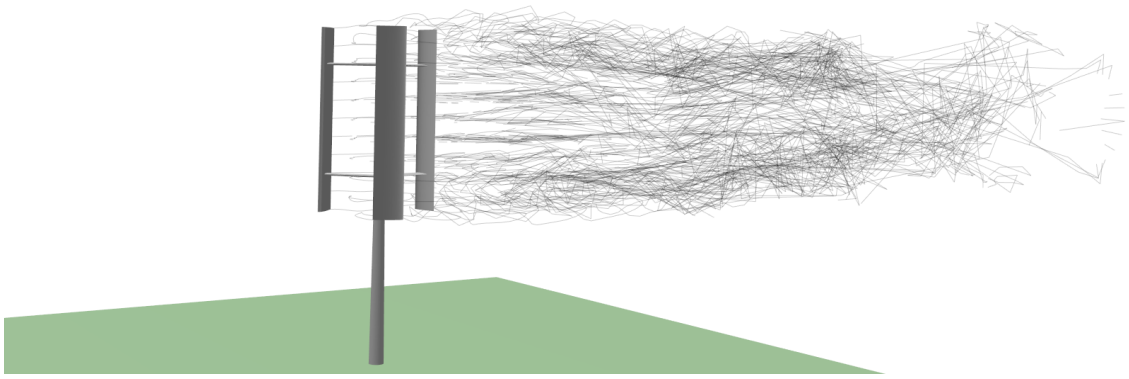

Figure 2.2: Qblade simulation environment

The turbine was numerically simulated to assess its aerodynamic performance and evaluation using QBlade Community Edition, a software license under the Non-Commercial Academic Public License [9]. This advanced wind turbine simulation tool encompasses airfoil analysis, 360-degree polar extrapolation, definition of rotor blades and struts, simulation based on the double multiple stream tube model, and stages for defining and simulating vertical-axis wind turbines.

2.1.2 Filament processing

A modified Hummer method was utilized to synthesize monolayers of graphene oxide starting from natural flake graphite, as previously reported by our group [10]. The polymer matrix and graphene oxide were mixed uniformly within the twin screw chamber of the Xplore Micro Compounder MC 5. [11] This extrusion device accommodates sample sizes of up to 5 ml and exerts a maximum torque of 6 Nm. Its chamber temperature can be precisely regulated up to a maximum of 450 degrees Celsius, facilitated by an automatic cooling system utilizing either water or air.

The extruded polymer filament is gathered by the Xplore winding unit [12], as depicted in Figure 2.3. This unit governs the rate at which filament is drawn from the extruder chamber. By adjusting the torque applied to the filament, the diameter of the filament can be varied.

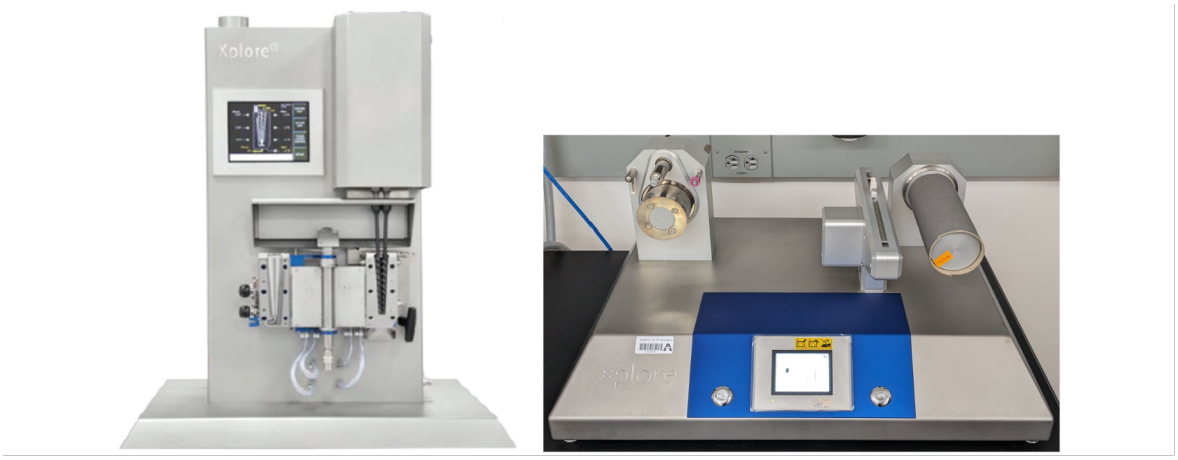

Figure 2.3: Filament extrusion and winding units

2.1.3 Computer aided design and structural analysis

A computer-aided design (CAD) model of a vertical axis wind turbine was crafted using Onshape [13], a cloud-based modeling platform accessible through a student education account. A parametric design was developed to facilitate swift modifications based on feedback from structural analysis.

Subsequently, the design model was imported into Ansys Workbench [14], a licensed software, within the CAD laboratory of the Department of Mechanical and Aerospace Engineering at the University of Texas at Arlington. Within this analysis environment, simulation constraints such as boundary conditions and load directions were defined. Results were then computed and visualized using the static structural mode.

2.1.4 Data plots

Graphical representations and analyses of generated data, including centrifugal forces, tensile test outcomes, aerodynamic coefficients, and forces, were conducted using MATLAB version 23.2.0.2485118 (R2023b) Update 6 under a valid license [15]. This software facilitated comprehensive visualization and examination of the data to derive insights and conclusions.

2.1.5 Tensile testing

Figure 2.4: Tensile test equipment

Filament tensile tests were performed using the Shimadzu AG-X plus 10 kN tabletop model, as documented by Shimadzu [16]. To ensure accurate measurements, a 1 kN load cell was affixed, and custom mounting tabs specifically designed for filament testing were employed.

CHAPTER 3

GRAPHENE REINFORCED POLYETHYLENE TEREPHTHALATE

3.1 Polymer synthesis

3.1.1 Recycling

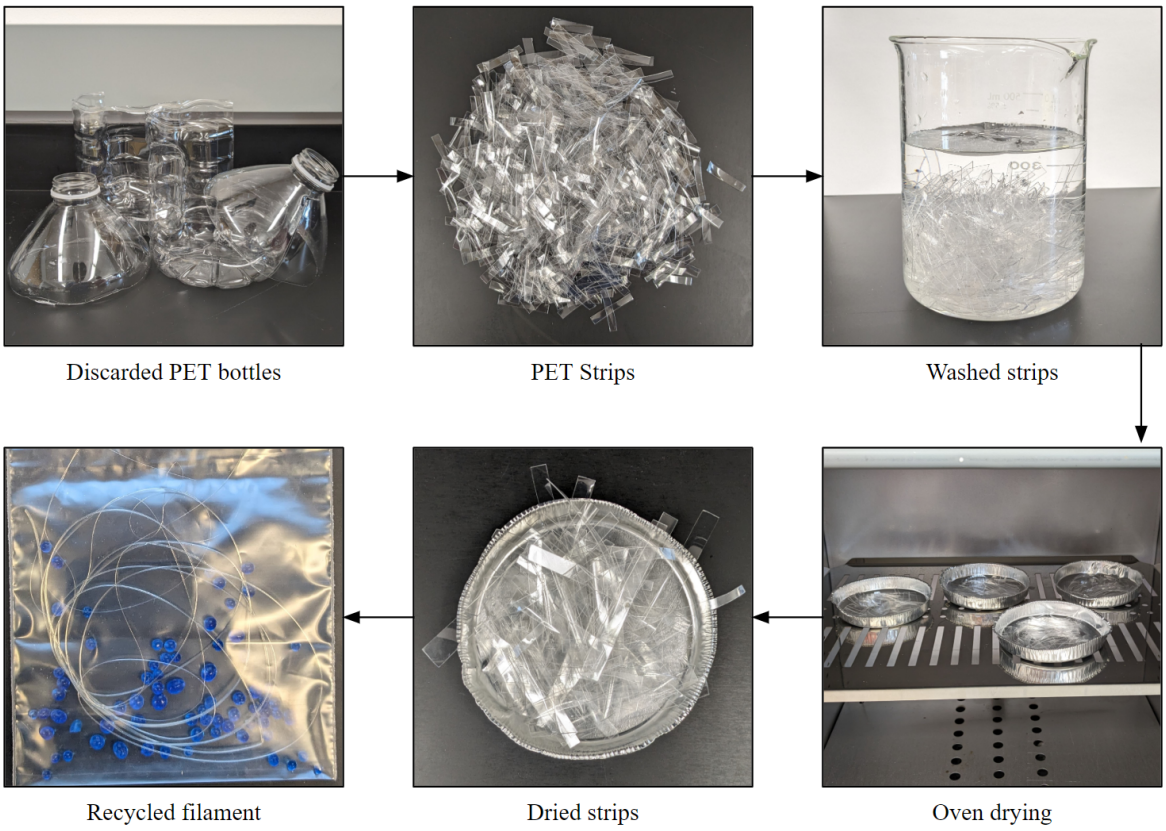

Figure 3.1: Discarded PET bottles recycling

Discarded PET bottles are processed into strips of approximately 3 cm length and 1 cm width. This size ensures easy feeding of Polymer material inside the extrusion chamber. These PET strips undergo a thorough cleansing with a solution of ethanol and distilled water to eliminate impurities, particularly adhesive residues from labels adhered to the bottles.

Subsequently, the strips were immersed in a solution of distilled water and ethanol, with a 1:1 ratio, for a soaking duration of 24 hours. Subsequently, the strips are placed in an oven set at 50 °C, a temperature below the glass transition temperature of polyethylene terephthalate, which typically ranges between 60 and 80 °C.

The term ”glass transition temperature” (Tg) denotes the temperature at which an amorphous solid material transitions from a rigid state to a more pliable state resembling a supercooled liquid. This transition occurs as the molecular bonds within the material become less rigid and more mobile. By drying the strips below this threshold temperature, which might cause contraction or expansion, their original shape is preserved. Once dried, the PET strips are ready to be introduced into the extrusion chamber.

3.1.2 Filament extrusion and winding

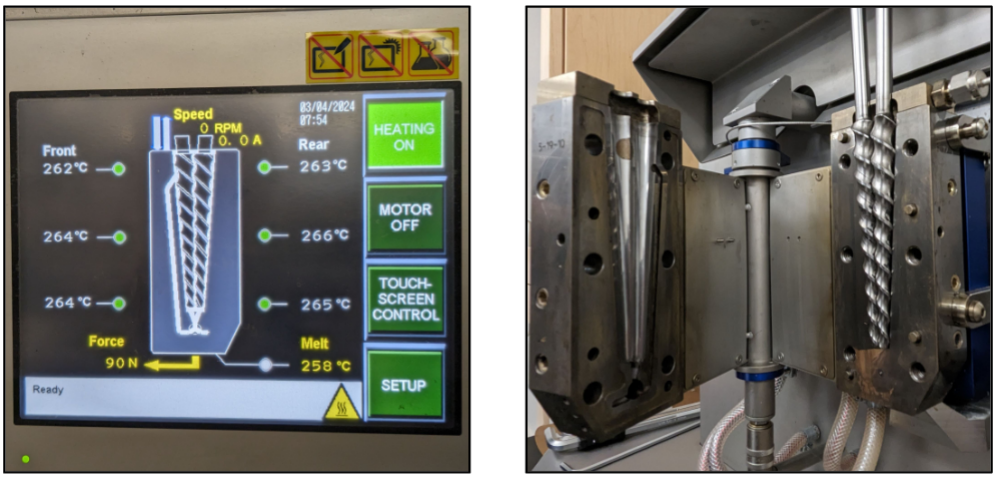

Chamber controls Twin screw

Figure 3.2: Extrusion chamber and control parameters

The extrusion machine comprises a heated chamber that houses a rotating twin screw assembly designed to melt and propel polymer material. Polymer can be introduced into the chamber via a hopper attachment, accommodating either pellets or shredded polymer pieces. Alternatively, strips can be fed directly into the chamber by removing the hopper.

Equipped with six temperature sensors positioned at various points, the chamber features internal channels for either water or air cooling should the temperature surpass the predefined threshold. At the chamber's base lies a valve capable of rotating 180°: when closed, it facilitates polymer recirculation near the feed point, and when open, it allows polymer to exit the chamber via a nozzle. The rotation speed of the twin screws is controlled in revolutions per minute (rpm), with higher rpm ensuring homogeneous polymer mixing and lower rpm facilitating extrusion through the valve.

Initially, the chamber is heated to the melting temperature of polyethylene terephthalate, which typically varies between 250 and 265 °C. Once the internal temperature reaches the desired level, PET strips are fed into the chamber through the hopper opening, one by one. As the polymer melts, the rotating screws push it downward through the chamber. The Microcompunder MC-5 has a maximum sample size of 5 ml, the quantity of PET strips inserted is adjusted accordingly.

Following the melting of PET strips, graphene oxide nanoparticles are introduced into the chamber, where they are uniformly dispersed within the polymer matrix by the rotating twin screws. Subsequently, the rpm is reduced to facilitate extrusion of the reinforced polymer through the bottom nozzle by opening the valve. The extruded polymer undergoes rapid cooling upon exposure to ambient temperature. It is then guided over a godget and passed through a series of notches and rotating cylinders to be collected as a filament.

The winding unit features two distinct rotating cylinders utilized to control the diameter of the extruded filament. The first set of rollers regulates the speed of filament pulling in millimeters per minute and incorporates an air cooling system to solidify the filament. The second rolling cylinder, torque-controlled, further draws the filament on top itself. By defining these two parameters, speed and torque, precise control over the filament diameter is achieved.

3.2 Material testing

3.2.1 Tensile testing

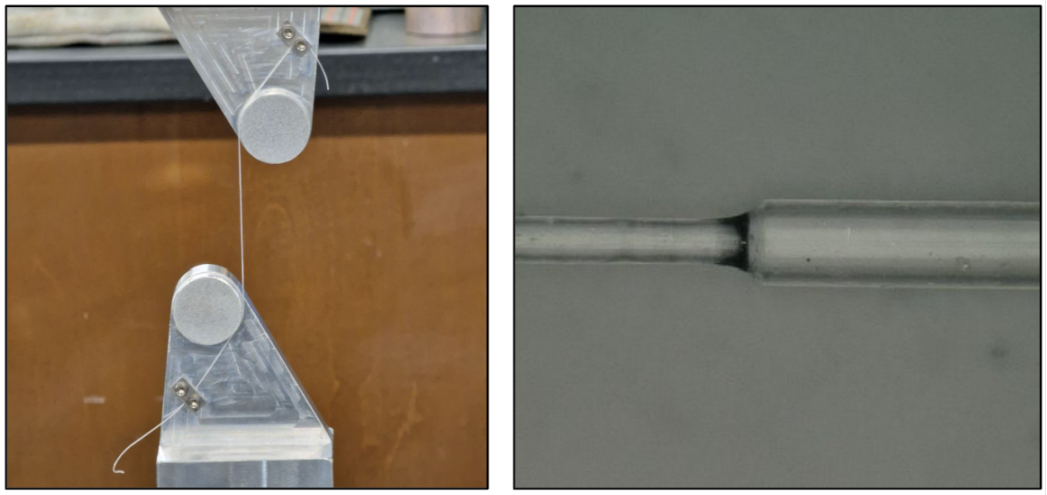

Tensile test setup Filament necking

Figure 3.3: Filament under tensile loading

Test specimens of PET filament, approximately 30 cm in length with a diameter tolerance of approximately 20 μm, were obtained from a winding roll spool for tensile loading experiments. The majority of the filament's length was used to secure it onto the mounting tabs of the testing apparatus. Initially, one end of the filament was anchored against a mounting tab using a screw-tightened flange to ensure stability, while the remaining portion was wound around circular tabs of the tensile test attachment. The other end of the filament was fixed in place similarly with a screw-tightened flange. This arrangement ensured that the filament experienced tension only within the gauge length segment.

The tests were carried out according to the ASTM C1557-20 standard for tensile testing [17]. The gauge length represents the section of the filament free to undergo tension on the testing machine. Considering PET's elongation characteristics, the initial gauge length was uniformly set at 1 cm for all tests. Failure of the test was defined as the filament breaking outside of this predetermined region.

During the test, the upper tab was displaced at a constant rate of 250 mm/min, while the lower tab remained stationary. The filament resisted this displacement and the resulting force was captured by the load cell positioned above the top mounting tab. As the applied tensile load increased, the stress within the filament increased, reaching its yield stress value as detailed in figure 3.3. At this juncture, the filament begins to deform beyond its elastic limit and continues to yield until eventual tensile failure.

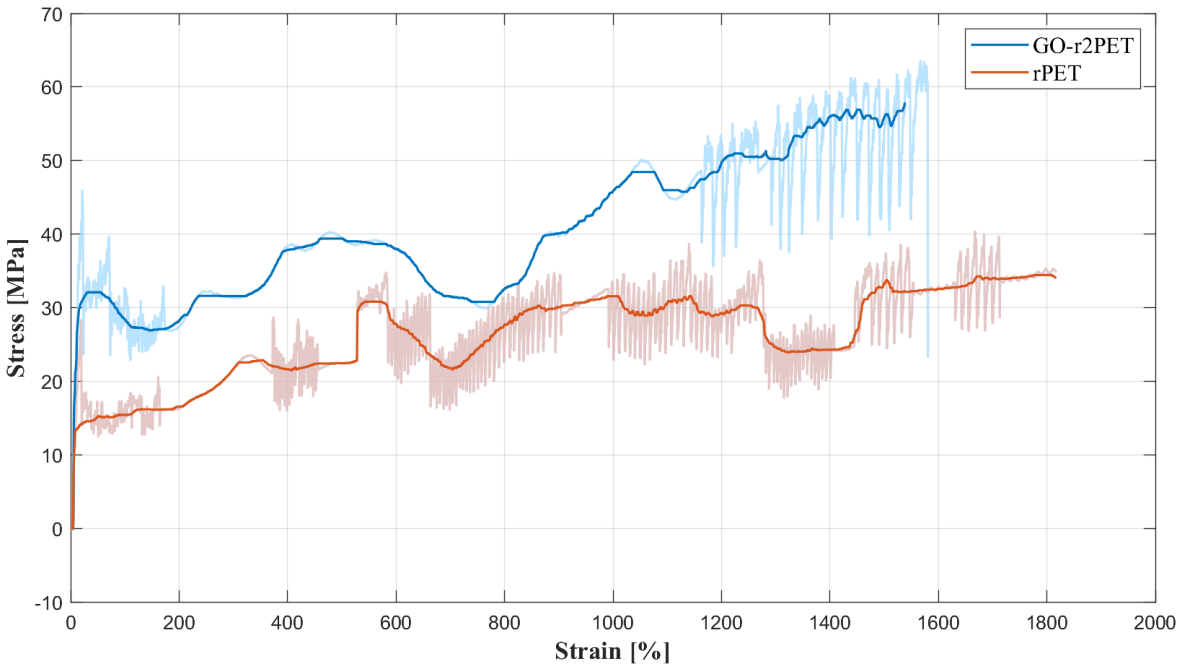

Figure 3.4: Recycled and reinforced rPET stress-strain curve

The behavior of recycled PET filament (depicted in orange) and recycled PET reinforced with graphene oxide nanoparticles (shown in blue) is illustrated in Figure 3.4. Noticeable distinctions are evident in both tensile yield strength and ultimate tensile strength, along with slight alterations in elongation at break. As the applied load surpasses the elastic limit, polymer chains gradually align in the direction of the force, thereby augmenting the filament's capacity to endure higher stress levels.

The translucent plot depicts the raw test data. The outer layers of filaments exposed to ambient airflow cool at a faster rate than the filament core. As a consequence of effective

heat treatment, the outer surfaces become slightly harder while the inner sections remain softer, and the change in rate of cooling potentially leads to sliding between these layers during tensile testing. This phenomenon induces slipping between the various layers of the filament. Nevertheless, the effective filtered stress-strain curve illustrates the positive change in Tensile strength, Modulus of Rigidity, and decrease in elongation at break.

A similar research study where Graphene nanocomposites underwent melt compounding on an internal mixer, following which the resultant materials were compression molded into films [18]. at a minimal nanofiller load of 0.07 weight percentage, these nancomposite material demonstrated over a 10 percent increase in elastic modulus and a more than 40 percent enhancement in tensile strength when compared to pristine PET.

3.2.2 Differential Scanning Calorimetry (DSC)

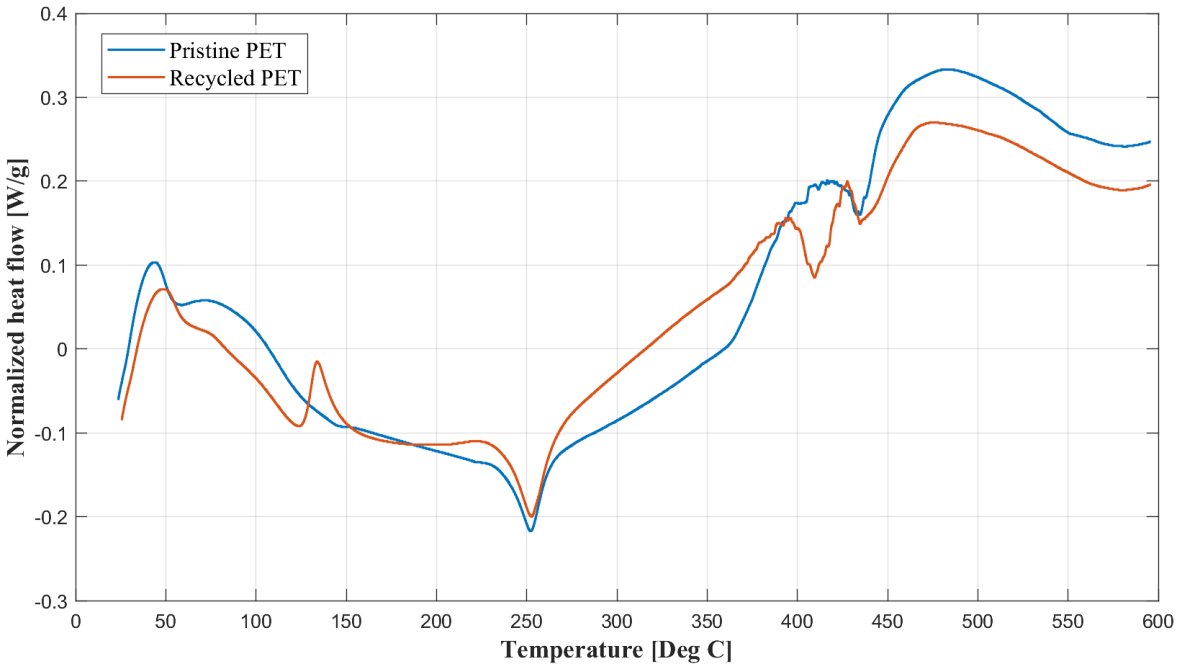

Figure 3.5: Differential scanning calorimetry - pristine and recycled PET

The differential scanning calimetry (DSC) graph compares the thermal properties of Pristine PET (blue line) and recycled PET (orange line).

Both materials exhibit a glass transition region, which appears as a step in the heat flow curve. This is the range where the PET material transitions from a glassy to a rubbery state. The close proximity of T_g for both samples indicates that the recycling process has not significantly altered the glass transition temperature.

Following the glass transition, both curves show an exothermic peak, indicating cold crystallization. The recycled PET exhibits this peak at a slightly lower temperature than the virgin PET, which suggests a different crystalline structure or a higher amount of crystallizable material in the recycled sample.

Both samples show a clear endothermic peak corresponding to the melting point. The recycled PET has a melting peak that is slightly broader and shifted to a lower temperature compared to the virgin PET. This suggests that the recycled material may have a more diverse range of crystallite sizes or less perfect crystals.

The area under the melting peak correlates with the degree of crystallinity. If the area under the recycled PET's peak is less than that of the pristine PET, this indicates lower crystallinity, which is common in recycled materials due to thermal and mechanical degradation.

Thermal degradation of pet typical occurs above 350 °C PET degradation range, Both samples show similar thermal behavior, but the slight differences in the cold crystallization and melting behaviors suggest that the recycling process may introduce some variability in the physical properties of the PET.

3.2.3 Fourier Transform Infrared Spectroscopy (FTIR)

Both pristine and recycled PET show very similar peaks, suggesting that the fundamental chemical structures remain largely unchanged after recycling. This is expected as PET is a thermoplastic and can retain its properties upon remelting and reshaping.

There may be slight differences in the intensity of the peaks between the pristine and recycled PET. These differences could be due to varying concentrations of PET in the sam-

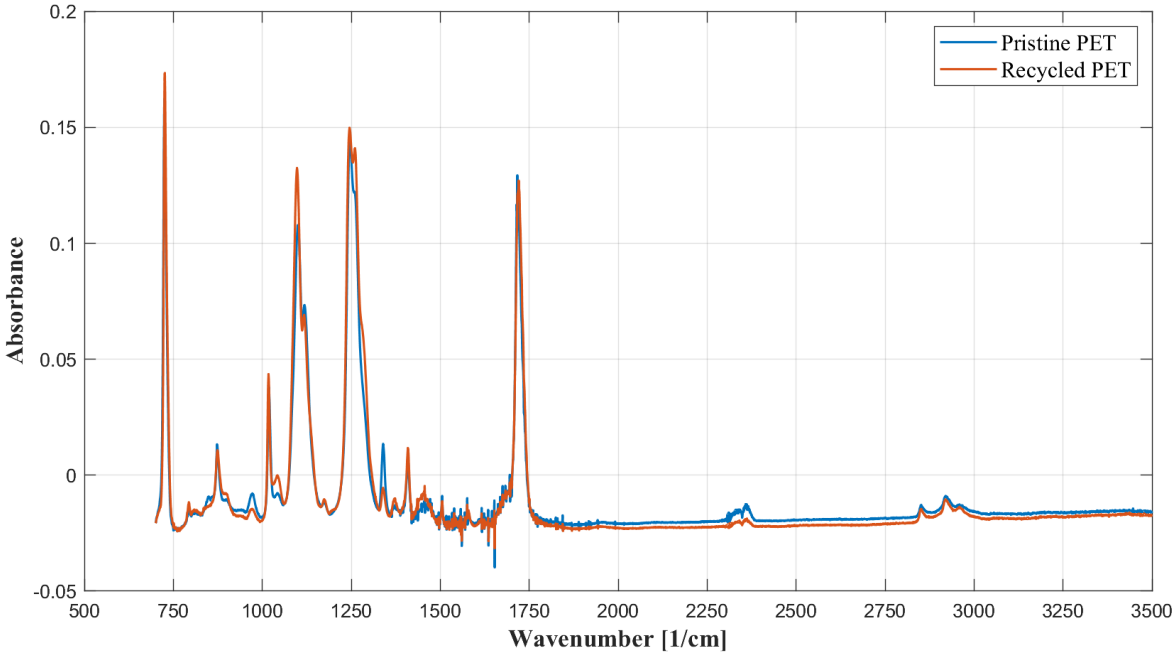

Figure 3.6: Fourier Transform Infrared Spectroscopy - pristine and recycled PET

ples or minor changes in the chemical structure due to the recycling process. Small shifts in some of the absorbance peaks indicate some level of degradation or chemical modification of the PET during the recycling process. Any additional peaks present in the recycled PET but not in the pristine PET suggest the presence of impurities or additives introduced during the recycling process. The absorbance values for both types of PET are relatively low and the overall profile of the spectra is very similar, which suggests that the recycled PET retains most of the characteristics of the pristine material.

CHAPTER 4

DESIGN, PERFORMANCE AND ANALYSIS OF VAWT

4.1 General mathematical expressions

The two key dimensionless parameters are Tip speed ratio (TSR) (equation 4.1) and Solidity factor (σ) (equation 4.2). TSR is defined as a ratio of blade speed ($R\omega$) to the free-stream velocity. Different rotor designs have specific optimal range of Tip Speed Ratios within which rotors generates energy at maximum efficiency.

$$TSR = \frac{R\omega}{V_\infty} \tag{4.1}$$

Solidity is a function of number of blades, chord length of blade foils and diameter of rotor. It represents a fraction of area swept by rotor blades with respect to total frontal area of the turbine rotor. In general, higher solidity value means that the rotor will generate significant torque at low wind speeds but with a downside of producing more drag. on the other hand, lower tip speed ratio means that the turbine is effective at high wind speeds but will struggle to pick up its rotational speed at lower wind speeds.

$$\sigma = \frac{NC}{D} \tag{4.2}$$

Figure 4.1 illustrates the breakdown of velocity components experienced by rotor blade as it moves. The velocity in the direction of the chord (V_c) is composed of the velocity of the blade and the component of the induced velocity. On the other hand, Velocity normal to the chord only has a component of induced velocity.

$$V_c = R\omega + V_i cos\theta \tag{4.3}$$

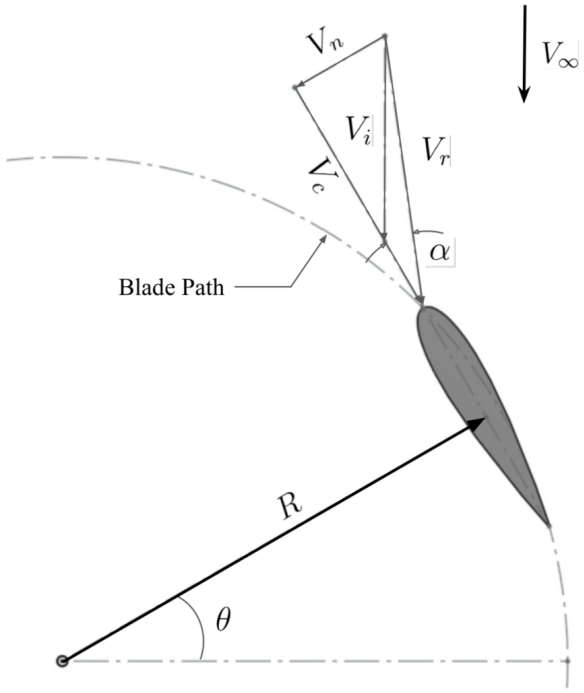

Figure 4.1: Velocity components on VAWT blade

$$V_n = V_i sin\theta \tag{4.4}$$

Angle of attack on the blade foil is given below. It can further be simplified by substituting values from equation 4.3, 4.4 and non-dimensionalizing with respect to free stream velocity.

$$\alpha = \arctan\left(\frac{V_n}{V_c}\right) \tag{4.5}$$

$$\alpha = \arctan\left[\frac{sin\theta}{\frac{TSR}{(V_i/V_\infty)} + cos\theta}\right] \tag{4.6}$$

The rotating blade experiences velocity relative to chordal and normal velocities which is expressed as follows. It can be further deduced by substituting values of V_c, V_n and non-dimensionalizing with free stream velocity.

$$V_r = \sqrt{{V_c}^2 + {V_n}^2} \tag{4.7}$$

$$V_r = V_i\sqrt{\left[\frac{TSR}{V_i/V_\infty} + cos\theta\right]^2 + sin^2\theta} \tag{4.8}$$

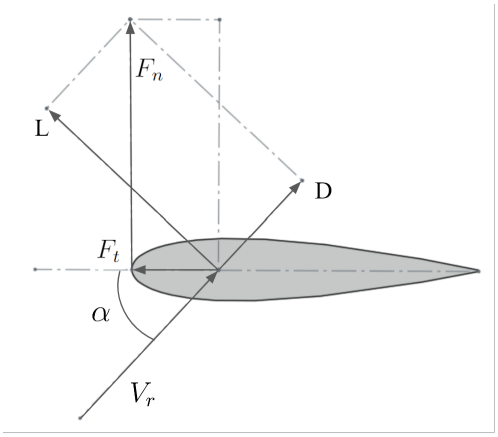

Figure 4.2: Relative airflow and lift, drag components

Resultant tangential and normal forces require coefficient of tangential force (C_t) and coefficient of normal force (C_n) given below. These coefficients depend on preliminary airfoil characteristics such as coefficient of lift (C_l) and coefficient of drag (C_d). At a given azimuthal angle of rotating blade, resultant normal and tangential forces are a function of chorld length (C), Blade Height (H), relative velocity of blade (V_r), density of air (ρ) and force coefficients.

$$C_t = C_l sin\alpha - C_d cos\alpha \tag{4.9}$$

$$C_n = C_l cos\alpha + C_d sin\alpha \tag{4.10}$$

$$F_t = C_t \frac{1}{2}\rho C H {V_r}^2 \tag{4.11}$$

$$F_n = C_n \frac{1}{2}\rho C H {V_r}^2 \tag{4.12}$$

Average tangential force which generates torque on the rotor by one blade in one complete revolution can then be computed by following equation.

$$F_{tan} = \frac{1}{2\pi} \int_0^{2\pi} F_t(\theta)\, d\theta \tag{4.13}$$

Consecutively, Total Torque (T) due to number of blades and their radial distance and total power (P) can be expressed by equation (3.14) and (3.15).

$$T = N F_{tan} R \tag{4.14}$$

$$P = T\omega \tag{4.15}$$

4.1.1 Induced velocity

Several computational models have been developed to predict the induced velocity and performance of the rotor. This study uses the double multiple stream tube momentum model which provides better correlation between computed and test results compared to single stream tube or multiple stream tube momentum models [19].

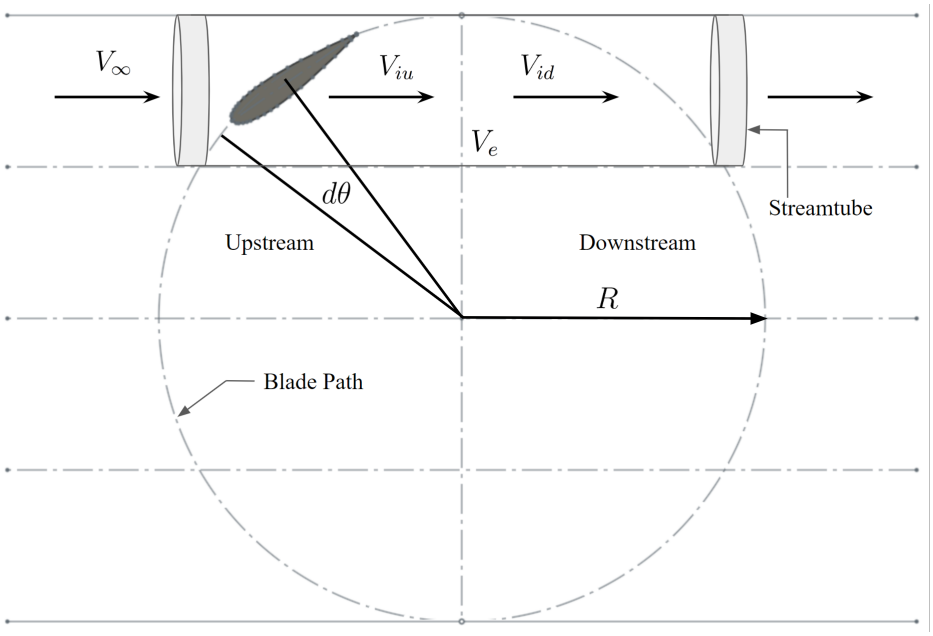

Figure 4.3: Momentum model: Double multible stream tube

Double multiple stream tube model considers in-viscid and in-compressible airflow to determine upstream, downstream and equilibrium velocities discussed below. DMST model divides the flow through the rotor in number of parallel streams. These aerodynamically independent stream tubes are further divided into upstream and downstream halves at the center as illustrated in figure 4.3. Conservation of momentum and blade element theories are employed in each stream-tube to calculate local induces velocities.

$$V_{iu} = uV_{\infty} \tag{4.16}$$

$$V_e = (2u - 1)V_{\infty} \tag{4.17}$$

$$V_{id} = u\prime V_e \tag{4.18}$$

V_e is known as equilibrium velocity and is also referred to as wake velocity for upstream half cycle. The upstream induced velocity is calculated by multiplying the interference factor u by the free flow velocity. Interference factors are computed by iterating the equation 4.19 and 4.20 until numerical convergence is achieved. Initially, upstream interference factor is assumed to be 1 and then the expressions are iterated until the difference between two consecutive interference factors is less than 10^{-4}.

$$u = \frac{\pi}{F_u + \pi} \tag{4.19}$$

$$F_u = \frac{\sigma}{2\pi} \int_0^{\pi} \left(\frac{V_r}{V_{\infty}}\right)^2 |sec\theta|(C_n cos\theta - C_t sin\theta)\, d\theta \tag{4.20}$$

Downstream interference factor is iterated with a similar set of equation where the limits of integration are $(\pi \leq \theta \leq 2\pi)$. This converged value of the upstream interference factor is fed as the initial guess for the downstream induction factor, and the equations are iterated once again until convergence is achieved [20] [21].

4.2 Rotor geometric definition

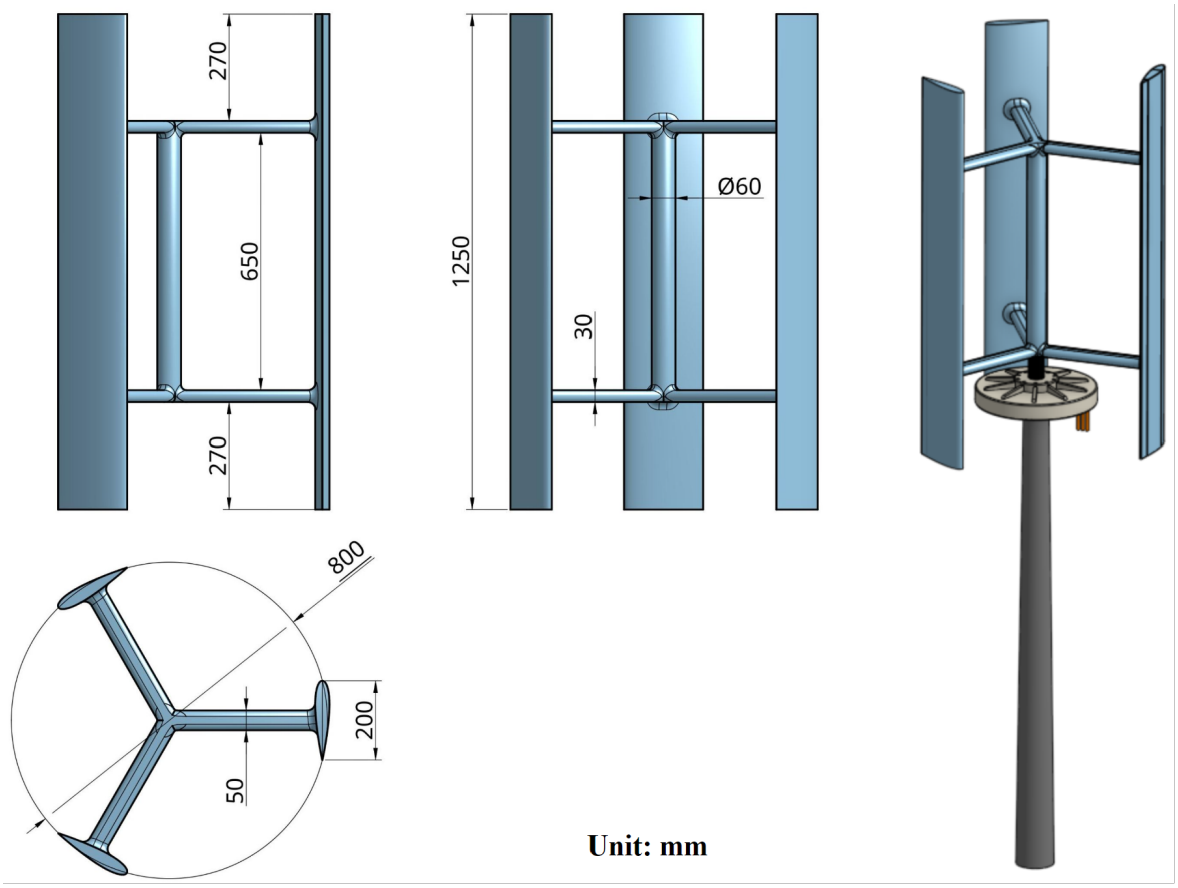

Figure 4.4: Turbine rotor geometric definition

The diagram above illustrates the geometric design of graphene reinforced polymer turbine. The rotor, in an H-blade configuration, comprises three blades measuring 0.8 meters in diameter and has a total height of 1.25 meters. Each blade incorporates two struts with an oval cross section, linking the rotor blades to the central shaft. These struts are in tension during turbine operation and aim to minimize outward blade deflection resulting from aerodynamic and centrifugal loads, elaborated extensively in the simulation section. The interfaces between the struts and blades have fillets with radii of 20 mm, whereas those between the struts and shafts have fillets measuring 14 mm in radius. The central shaft has a diameter of 60 mm, commensurate with the generator shaft for attachment.

$$P_w = \frac{1}{2}\rho dh{V_\infty}^3 \tag{4.21}$$

The amount of energy that can be extracted per second is directly related to the frontal area presented by the wind turbine. The diameter multiplied by the height of the rotor gives a swept area of 1 m^2, The maximum power available for the given rotor can be evaluated with 4.21. Remember that there exists a theoretical maximum limit for energy extraction (59.3%) from wind by any turbine and that is known as Betz limit [22]. More realistically, VAWTs operate in an even lower range of efficiencies 30% to 40% due to factors such as turbulence and environmental conditions.

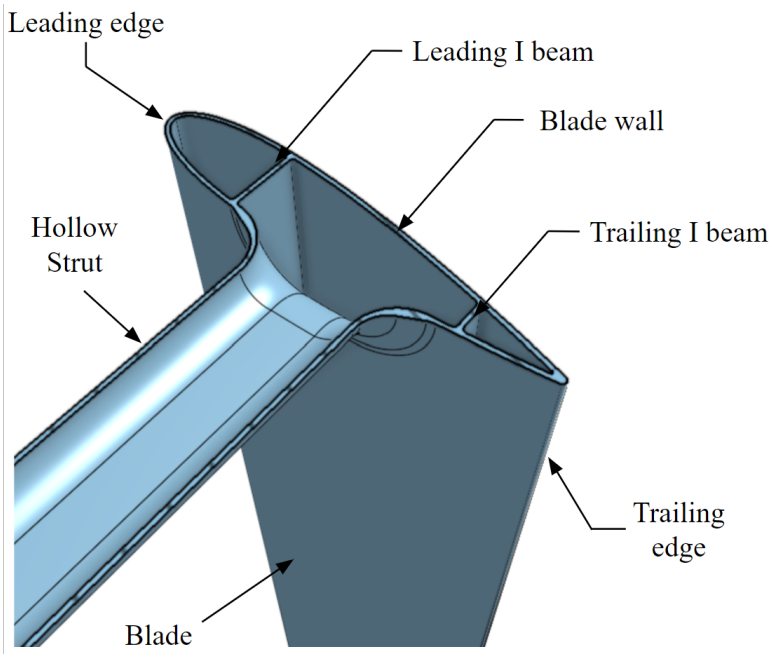

Figure 4.5: Section view of blade geometry - internal structure

The weight of the turbine rotor plays an important role due to two main factors. Firstly, a heavier blade mass increases rotational inertia, requiring more force to initiate turbine rotation. Secondly, once the rotation begins, the distribution of mass around the axis generates a centrifugal force. The higher mass further from the center increases this force. In both in-

stances of rotational inertia and resultant centrifugal force, it is advantageous for the turbine rotor to be as lightweight as feasible.

Design configuration	**Unit**	**Value**
Center of mass	m	0.3635
Total Mass	kg	1.894
Leading I beam	mm	2.2
Trailing I beam	mm	2
Blade wall	mm	2
Strut wall	mm	2
Trailing edge	mm	3

Table 4.1: Turbine blade computer aided design configuration

In this study, the hollow blade of the turbine rotor features two I beam structures, as illustrated in Figure 4.5. The primary load-bearing component is the leading I-beam, while the trailing I-beam serves to counteract deflection in the thinner (3mm wide) trailing edge of the blade. The leading I-beam has a thickness of 2.2 mm, with the remaining structure, including the blade walls, being 2mm thick. The radius of the interface between the strut and the blade experiences significant stress concentration and is reinforced with additional material thickness.

4.3 Aerodynamic performance analysis

4.3.1 Rotor blade airfoil

A symmetric airfoil NACA 0018 was chosen as a cross section of blades. The NACA 4-digit airfoil designation system is used for the classification of airfoil shapes. The first two digits specify the details of camber. In this case, there is no camber specified and consequently, the airfoil is symmetrical in shape. The last two digit specify maximum thickness as a percentage value of chord length. Cambered airfoils typically operate to maximize lift-to-drag ratio at

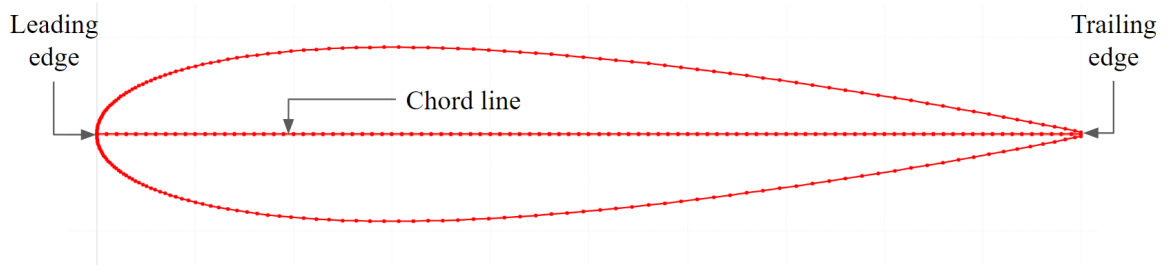

Figure 4.6: NACA 0018 - Blade cross section

specific angle of attack, and in case of VAWTs, blades are expected to operate at a wide range of angle of attacks. Symmetrical airfoils such as NACA 0018 perform well providing bidirectional efficiency making them suitable for this particular application.

Max. camber	**Max. thickness**	**Max. thickness location**	**Number of panels**
0%	18% of chord	30.6% of chord	200

Table 4.2: Airfoil parameters

The first step of the analysis is to determine key airfoil performance parameters such as Coefficient of lift (C_l), Coefficient of drag (C_d) and the moment coefficient (C_m). For this, airfoil analysis was carried out with the Reynolds number range of 100,000 to 400,000 while varying the angle of attack from -40 to +40 degrees with an increment of 0.1 degrees. Coefficient values as a function of angle of attack is plotted in figure 4.7.

It is observed that the boundary layer separates the surface of the airfoil at or near an angle of attack of 20 degrees. This is particularly visible in the above graphs as the data plotted becomes inconsistent. Even though the airfoil is analysed from -40 to +40 degrees, it is necessary at this stage to extrapolate possible airfoil performance beyond the range because the rotor blades may experience angles of attack well beyond the specific range during operation. To create 360 degree extrapolation from analysed airfoil performance, Montgomerie computational method was used [23]. This method assumes potential flow like behavior of airfoil at 0 degree angle of attack and basic thin plate like behaviour at

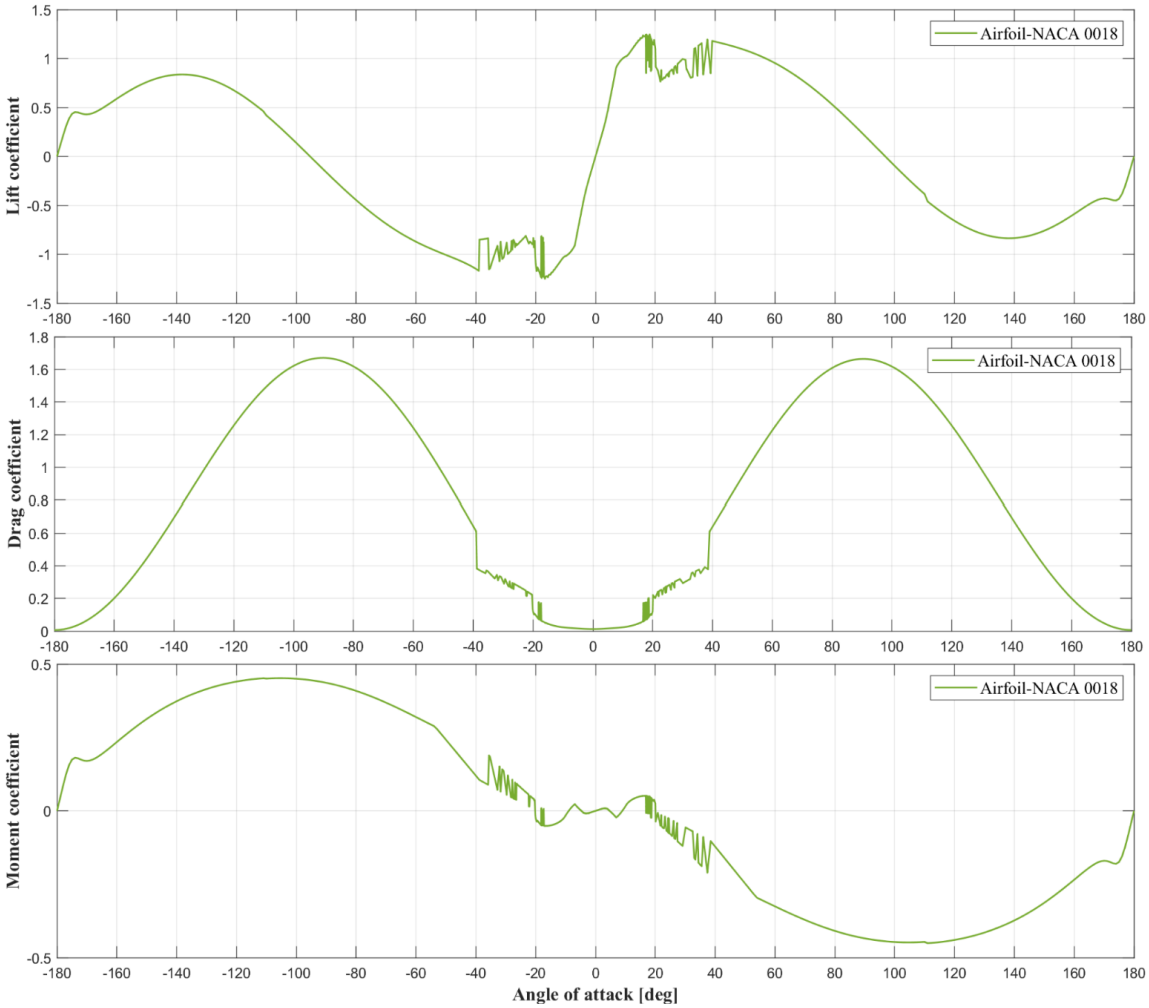

Figure 4.7: NACA 0018 Airfoil characteristics as a function of Angle of attack

higher angles of attack.

4.3.2 Steady double stream tube analysis

Double multiple stream tube analysis was performed for a wind speed of 8 m/s and 10 m/s for tip speed ratios ranging from 1 to 3 with an increment value of 0.1 TSR. Parameters assigned for this simulation are tabulated in table 4.3 below.

Parameters	Units	Value
Density	kg/m^3	1.184
Kinematic viscosity	m^2/s	0.00001562
Number of blade elements	-	25
Maximum number of iterations	-	1000

Table 4.3: Double multiple stream tube analysis parameters

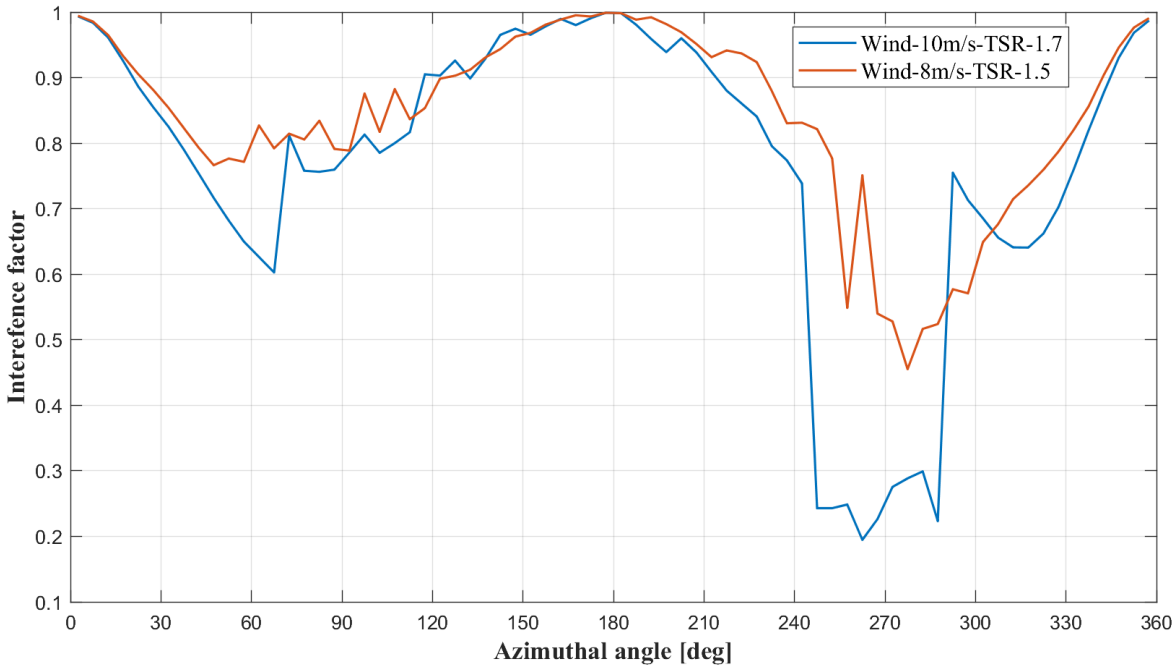

Figure 4.8: Change in interference factor [u] as a function of azimuthal angle[θ]

Interference factors

As discussed earlier in equations 4.19 and 4.20, the initial value of 1 is assumed and the consecutive interference factors are calculated by the iteration method until the variation in two consecutive values is very small. It should be noted that interference factors for the upstream half are higher than those for the downstream half. Since interference factor encompasses a ratio of relative velocity to free stream velocity, a similar trend is observed in both plots in figure 4.8.

Induced velocities

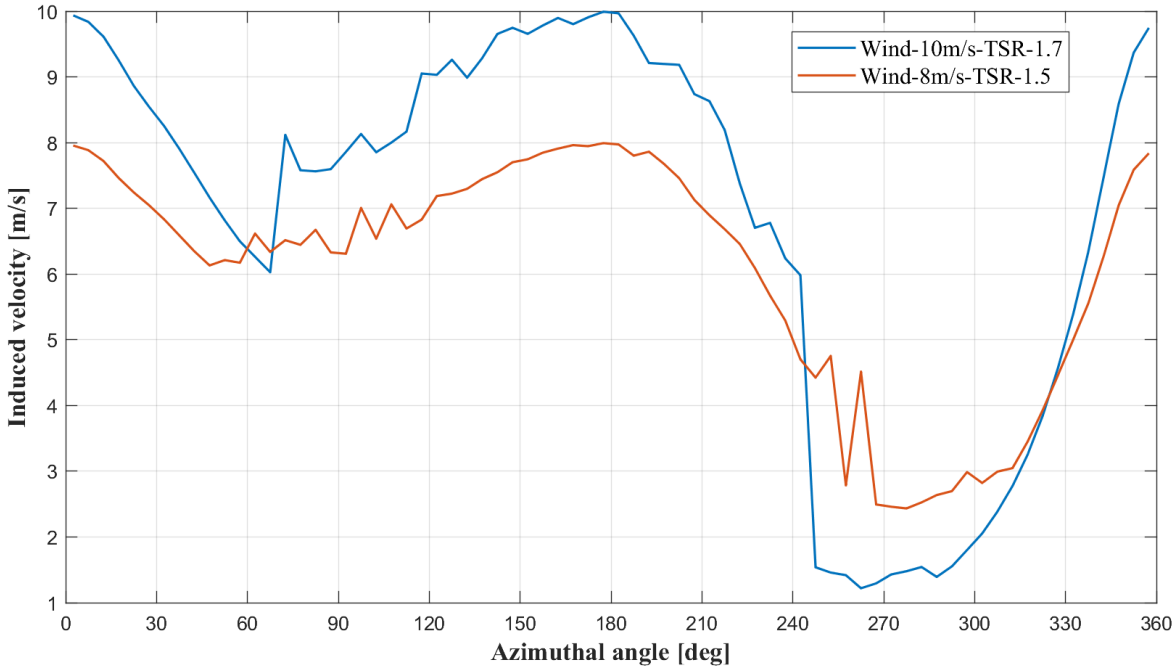

Figure 4.9: Change in induced velocity [V_i] as a function of azimuthal angle[θ]

Upstream induced velocity is computed by multiplying interference factor with free stream velocity as discussed in equations 4.16. when the value of the interference factor is assumed as 1 initially, the induced velocity is equal to the velocity of the free stream and so the plot in figure 4.9 begins at the design speeds. The effect of change in interference factor is noted thereafter as plot follows similar trend in figure 4.8. The values of equilibrium velocity and the downstream induce velocity are calculated based on the values of the upstream induced velocity as shown in equations 4.17, 4.18.

Considering chordal component and normal components of velocities and the effect of induced velocities result in actual velocity experienced by rotor blades. This resulting relative velocity interacts with blade geometry to produce lift and drag. When the blade is at 0 degree azimuthal angle, leading edge faces the incoming wind direction and hence, the maximum relative velocity is achieved. As the rotor spins and blade changes its azimuthal

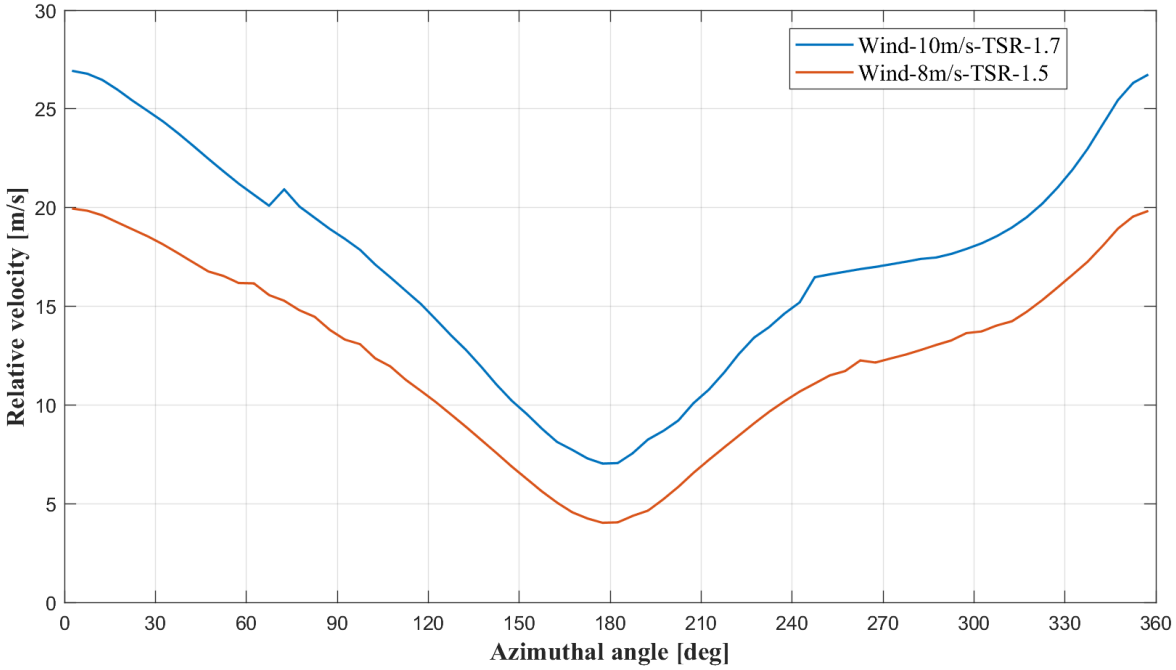

Figure 4.10: Change in total velocity of blade [V_r] as a function of azimuthal angle[θ]

position, the relative velocity decreases. When the blade reaches azimuthal angle of 180 degrees, trailing edge of the blade is facing the incoming wind flow and leading edge is facing in the direction of rotation and therefore, relative velocity reaches its minimum value.

VAWT rotor operates at wide range of angle of attack as shown in figure 4.11. As the blades spin faster, the range of angle of relative velocities, i.e. angle of attack of blade airfoil, reduces. This can be seen in the above plot where the blade rotating in 10 m/s wind speed with higher tip speed ratios limit the angle of attack range approximately from +32 to -25 degrees. However, the slow spinning turbine rotor reaches almost +38 in the upstream half-cycle and -30 in the downstream half-cycle. When the blade is at 0 degree azimuthal angle, the chord length of blade cross section is parallel to wind direction. Similarly, at 180 degree azimuthal angle, the blade is facing away from the wind flow with chord length parallel to it. Consequently, at both of these azimuthal locations of blade, angle of attack is 0 degrees.

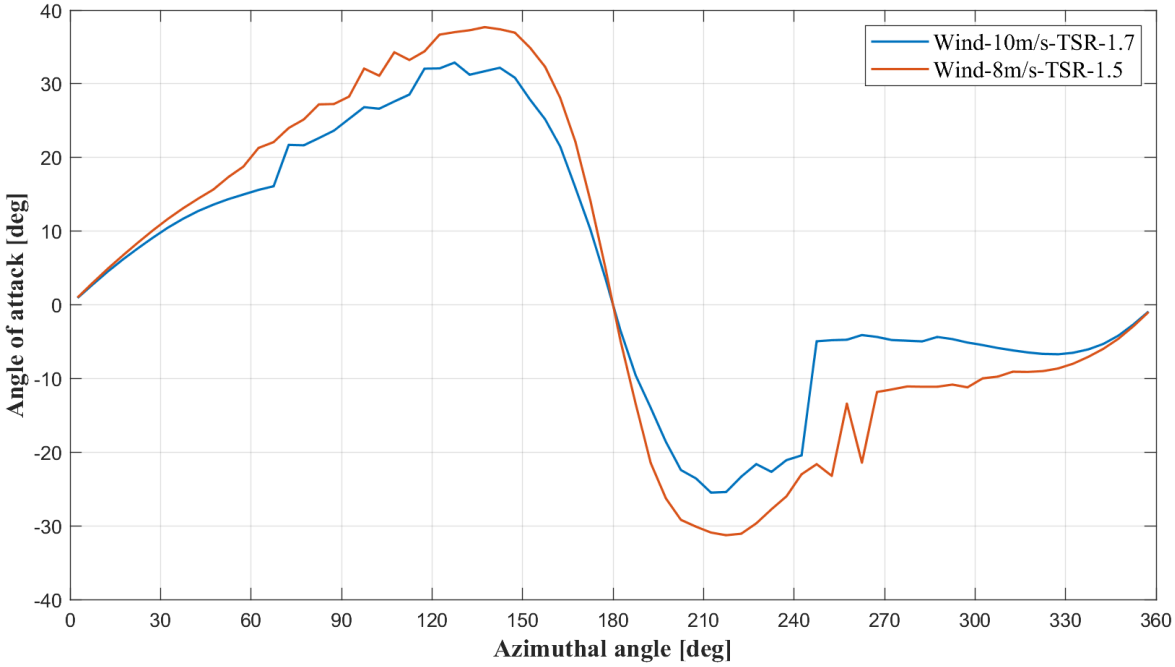

Figure 4.11: Change in Angle of attack of airfoil [α] as a function of azimuthal angle[θ]

4.3.3 Turbine definition and simulation

Turbine was defined in simulation environment with linear aerodynamic discretization of 10 panels on blade and 4 panels on struts. Structural model was turned off in order to focus solely on aerodynamic performance of turbine design. Table 4.4 holds the details of turbine definition with the wake type selected as free vortex.

Parameter	**Unit**	**Value**	**Parameter**	**Unit**	**Value**
Azimuthal step	deg	4	Ground clearance	m	1
Turbine Initial azimuth angle	deg	0	Tower height	m	1.2
Simulation length	s	1	Tower top radius	m	0.08
Gravity	m/s^2	9.806	Tower bottom radius	m	0.12
Air density	kg/m^3	1.184	X-tilt angle	deg	0
Kinematic viscosity Air	m^2/s	1.562e-05	Y-tilt angle	deg	0

Table 4.4: Turbine definition and aerodynamic simulation parameters

The turbine rotor defined above was simulated within mathematical models of turbine simulation software Qblade following the results of Double multiple stream tube analysis [19]. Considering the Average wind speed and maximum wind speed in Sudan as discussed earlier, a range of TSR values were simulated with initial condition of turbine as 0 degree azimuthal angle. As the simulation begins, the model solves for various parameters including tangential and normal force coefficients and forces generated by each blade. During simulation, the turbine rotor completes rotations within the defined simulation time of 1 second. Each iteration brings calculated values progressively closer together. The plots seen in figures 4.12, 4.13, 4.14, 4.15 represent converged values after the simulation is complete.

Coefficients and Aerodynamic forces

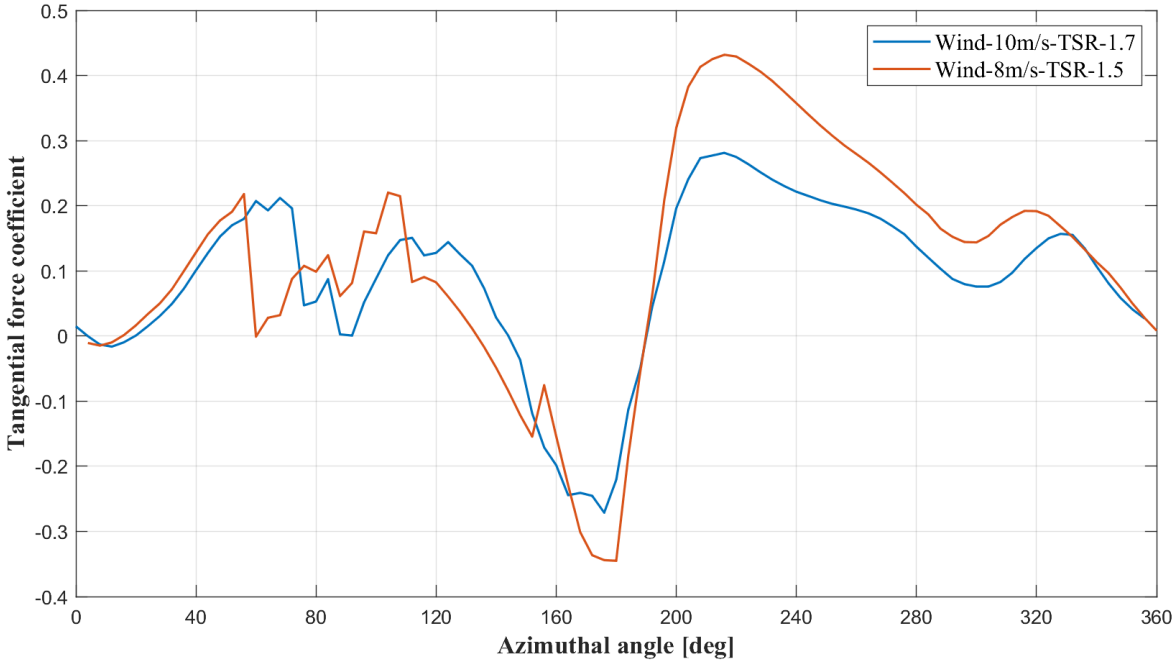

Figure 4.12: Coefficient of tangential force [C_t] as a function of azimuthal angle[θ]

Turbine blade rotating in the given wind speed generates lift and drag owing to the airfoil cross section. The lift force vector can be broken down into normal force and tangential force. The normal force acts radially outwards while tangential force contributes to genera-

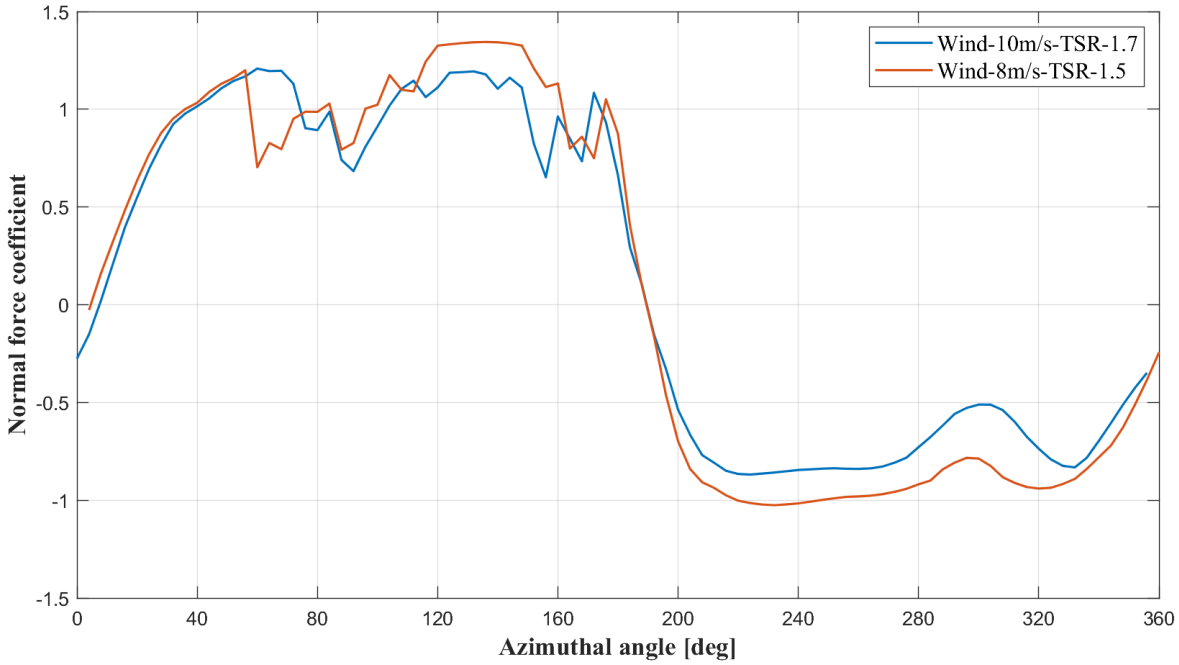

Figure 4.13: Coefficient of normal force [C_n] as a function of azimuthal angle[θ]

tion of torque which is pointed opposite to the drag force vector. Instantaneous magnitudes of these forces have been plotted in figure 4.15 and 4.14 as a function of azimuthal angles.

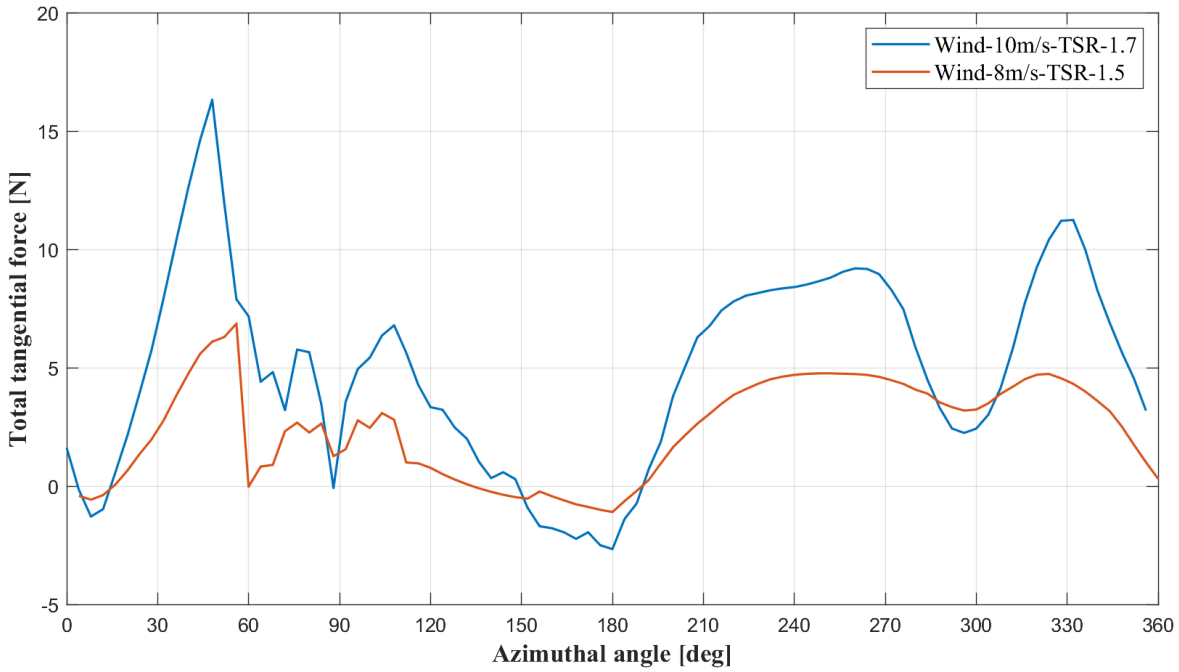

Figure 4.14: Total tangential force of single blade [F_t] as a function of azimuthal angle[θ]

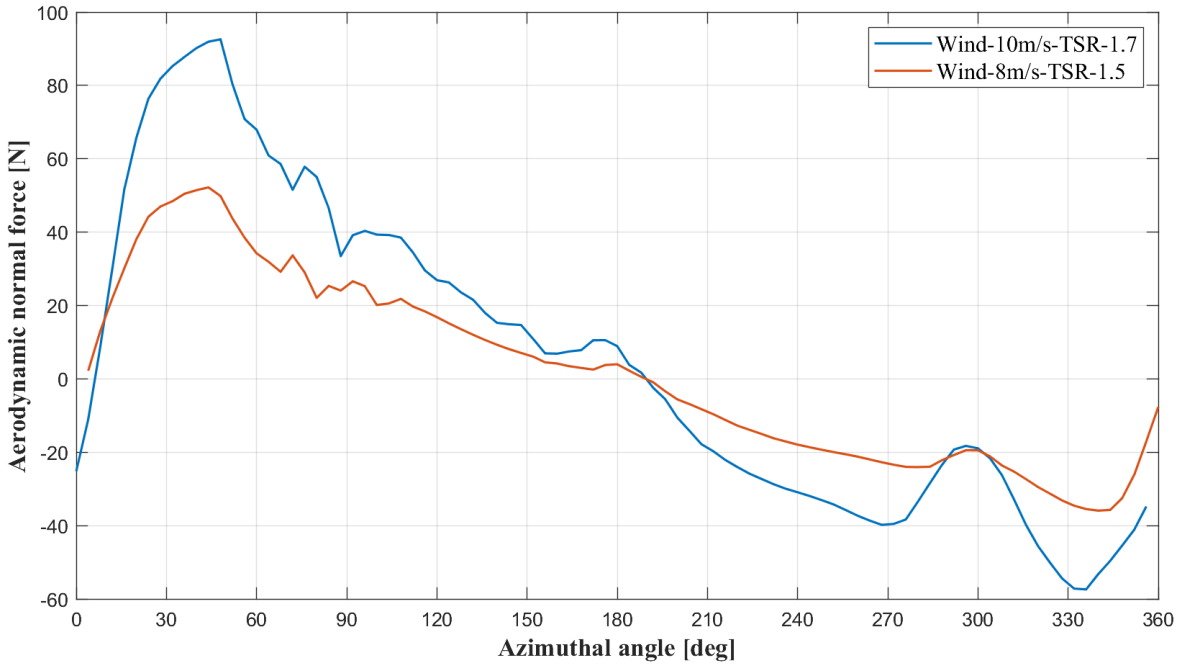

Figure 4.15: Aerodynamic normal load of single blade [F_n] as a function of Angle of attack

Aerodynamic power and coefficient of performance

Coefficient of performance of a turbine denotes the efficiency of turbine rotor to extract a fraction of power from total available wind power [24]. It can be evaluated with equation 4.22. The total available power for a turbine rotor is expressed in equation 4.21.

$$C_p = \frac{P}{P_w} \tag{4.22}$$

Aerodynamic power captured by turbine rotor is plotted against time in 4.16. and subsequently, Coefficient of performance is tabulated in table 4.5.

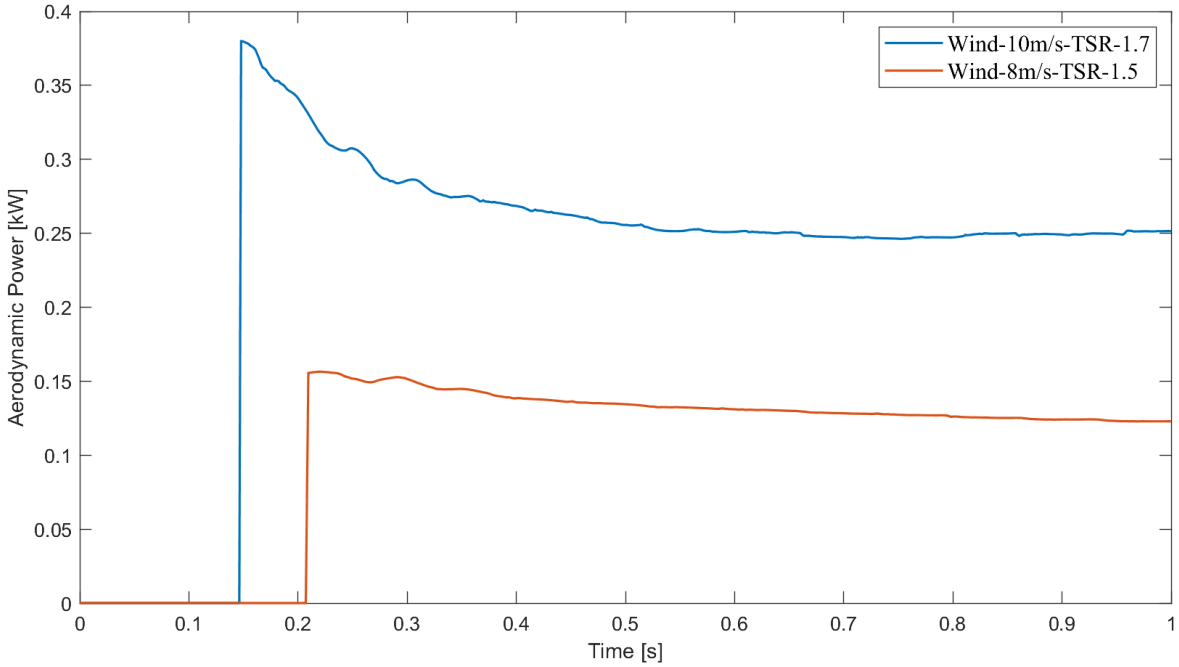

Figure 4.16: Turbine rotor coefficient of performance

Wind speed	TSR	P	Pw	Turbine efficiency
10 m/s	1.7	251 W	592 W	42.4 %
8 m/s	1.5	123 W	303 W	40.6 %

Table 4.5: Turbine rotor coefficient of performance

4.4 Rotor blade stress analysis

4.4.1 Maximum loading conditions

There are two main active loads acting on the rotor blades in an operating turbine. Aerodynamic loads generated by airfoil cross section of blade which results in tangential and normal force components discussed in figures 4.14 and 4.15 and centrifugal force generated by the blade's mass rotating around the central axis of rotation. Typically, the normal load resulting from blade aerodynamics is significantly lower than the load exerted by the blade's own rotational mass moving away from the center. This load aligns with the outward direction of the aerodynamic normal load and is essential to evaluate potential failure modes of turbine

blades.

The magnitude of centrifugal force acting on the turbine blade depends on it's mass, rotational speed and radial distance between axis of rotation and center of mass. It can be calculate by equation 4.23. Angular speed (ω) can be computed with the equation 4.24.

$$Centrifugalforce = M\omega^2 R \tag{4.23}$$

$$\omega = RPM * \frac{2\pi}{60} \tag{4.24}$$

For a given wind speed, and fixed Tip speed ratios, the turbine blade experiences constant magnitude of centrifugal force. The non linear relation between change in TSR and outward centrifugal force can be observed in 4.17. For the average wind speed case and maximum wind speed case, the details of centrifugal force considered are tabulated in table 4.6. For both cases, blade mass of 1.8945 kg and radial distance of 0.3635 m was considered as discussed earlier for blade model details in table 4.1.

Parameter	**Unit**	**Average wind condition**	**Maximum wind condition**
Wind speed	m/s	8	10
TSR	-	1.5	1.7
RPM	-	286.48	405.84
Blade azimuth angle	deg	44	48
Blade AOA	deg	14.8	13.6
Centrifugal force	N	619.78	1243.91
Aero. normal force	N	49.84	92.5
Total normal force	N	669.62	1336.41
Tangential force	N	5.58	16.31

Table 4.6: Maximum operating load on single blade

The constant centrifugal force in addition to aerodynamic normal force constitutes the total normal load exerted on the turbine blades. For the two cases discussed above, the

centrifugal force is combined with the aerodynamic normal force in figure 4.15 and the total resultant normal load is plotted against the azimuthal angle in figure 4.18.

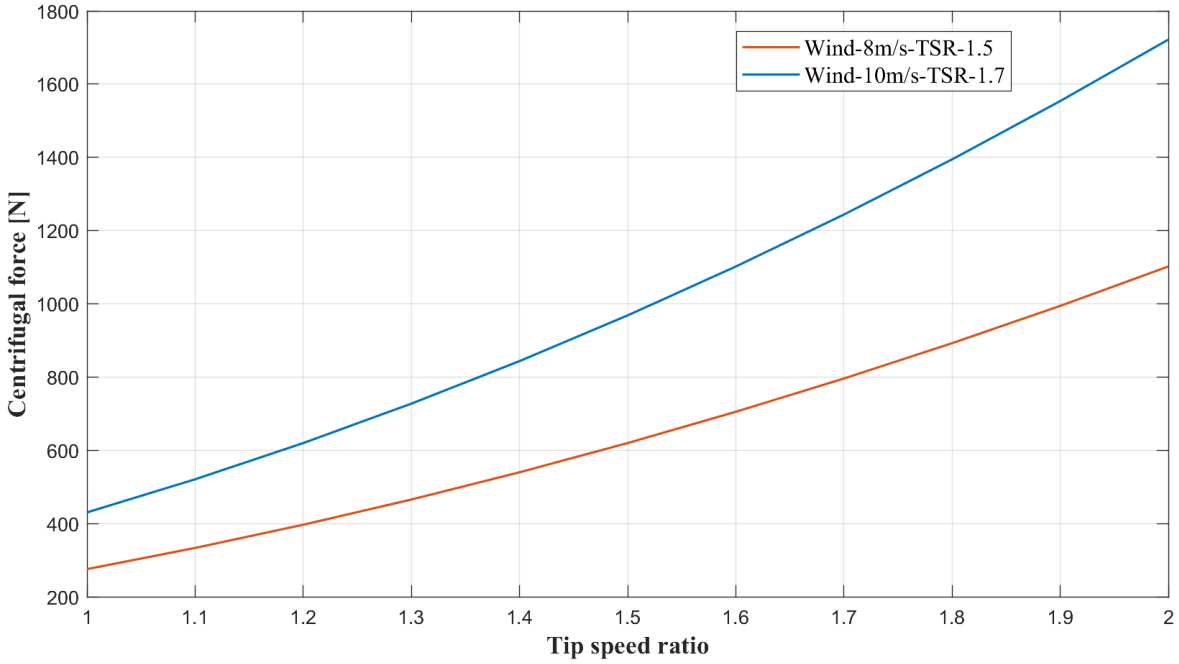

Figure 4.17: Centrifugal force as a function of Tip speed ratio

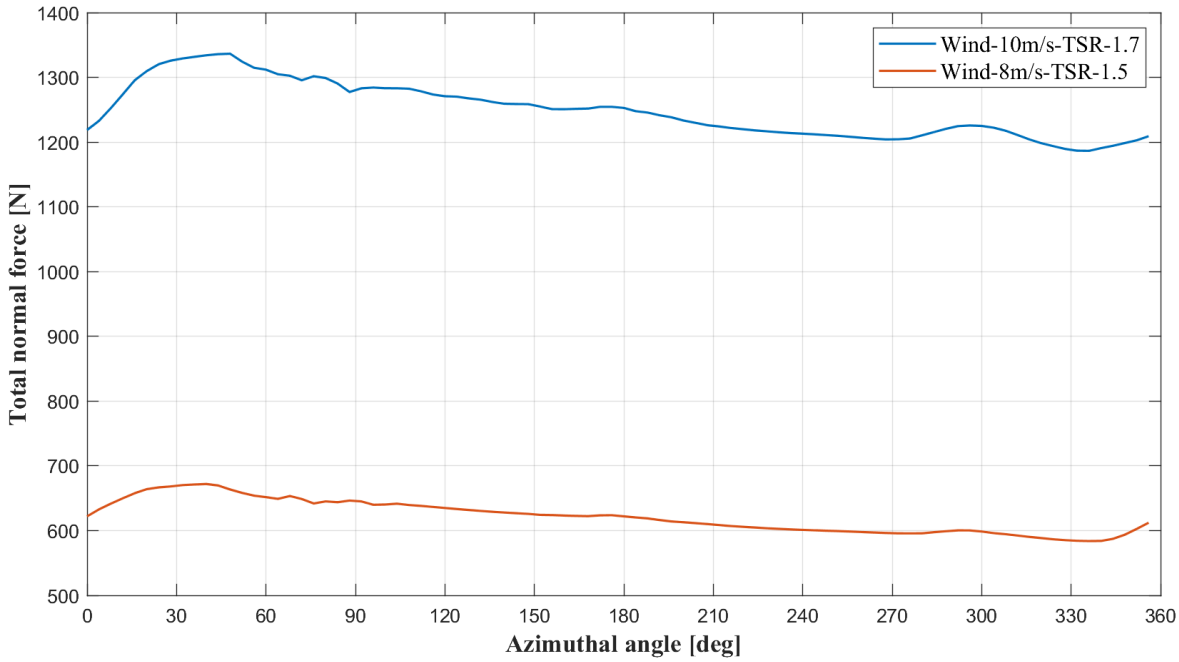

Figure 4.18: Total normal load on single blade as a function of Angle of attack

Total normal force on the turbine blade is two folds higher in maximum wind conditions compared to average wind speed conditions. This is because the centrifugal force is directly proportional to the square of the angular speed of the blades. Angular speed of blade at 10 m/s, TSR 1.7 is 40 rad/s, on the other hand, angular speed of blade rotating in 8 m/s wind speed at TSR 1.5 is 28 rad/s resulting in nearly half the load.

4.4.2 Analysis setup

The CAD model of the rotor was sliced precisely at the intersection point between the central shaft and the struts. This transformed single unified hollow blade body comprised of two struts and a blade. The model was exported from CAD environment and imported into analysis software with axis of struts parallel to the global X axis of analysis environment which ensured that blade spanned in Y direction. In this configuration, the faces of the struts were designated as fixed supports toward the end connected to the shaft and the surface of the rotor blade was subjected to two primary loads: an aerodynamic tangential load and a total normal load arising from both the blade aerodynamics and centrifugal force described in Table 4.6.

A tetrahedral mesh configuration with an element size of 5 mm was selected for the analysis model, as depicted in Figure 4.19. Utilizing adaptive mesh sizing with a coarse span angle center approach, an average surface area of 8.86E-03 m^2 and a minimum edge length of 0.41 mm were achieved. The resultant mesh structure comprised 174,140 nodes and 89,363 elements, effectively capturing the geometry of a 1250 mm long rotor blade with two struts. This mesh configuration balanced computational time with accuracy, ensuring precise simulations of structural behavior of the rotor blade.

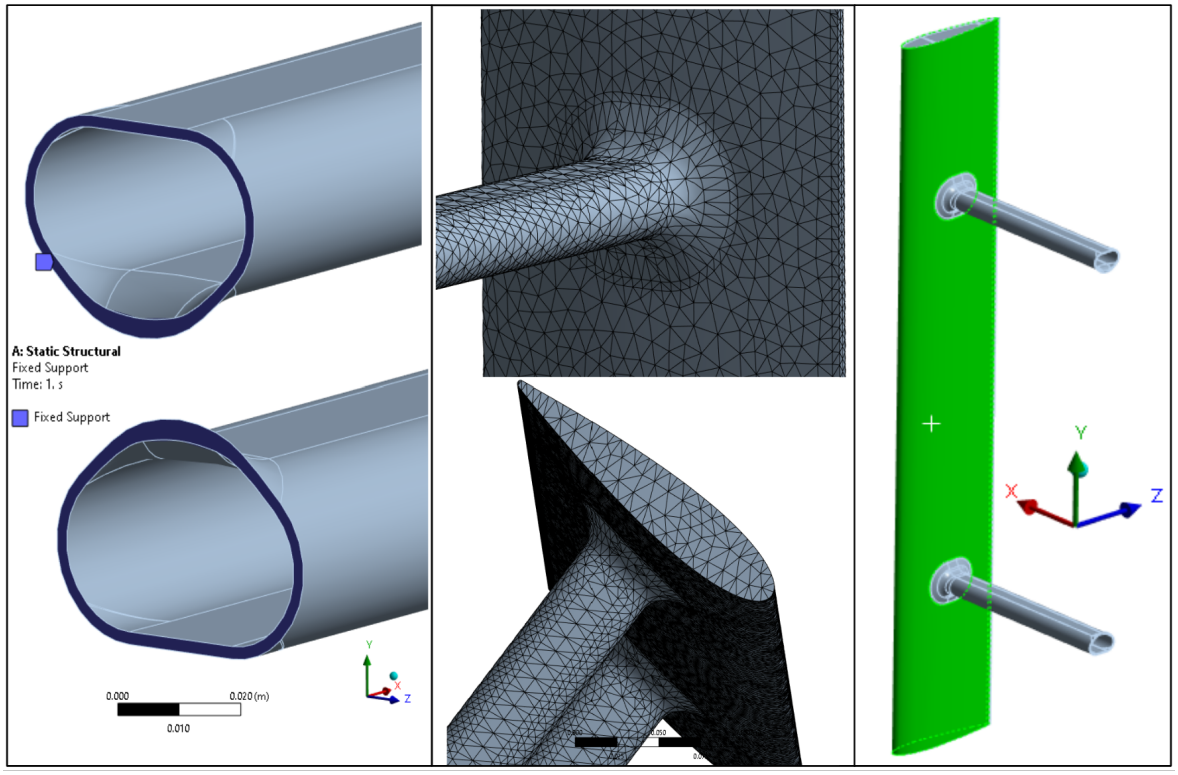

Figure 4.19: Mesh, fixed supports and loaded region

Engineering properties

Table 4.7 describes the properties of PET reinforced with graphene oxide used for analysis in this work [18]. The bulk modulus and shear modulus of PET are determined using Poisson's ratio and the modulus of elasticity.

4.4.3 Results

The stresses induced by operational loads under an 8m/s wind speed on a single turbine blade are depicted in Figure 4.21, showcasing their magnitudes and distribution. Predominantly, stresses accumulate at the interface where struts and blades meet. This phenomenon arises from the fixed position of one end of the strut coupled with the normal and tangential forces exerted on the blade. As the applied loads progress towards the fillet radius, they gradually

Property	Unit	Value
Melting temperature	Degree C	250
Glass transition temperature	Degree C	80
Density	g/cm^3	1.35
Young's Modulus	MPa	990
Poisson's ratio	-	0.37
Bulk Modulus	MPa	1269.2
Shear Modulus	MPa	361.3
Tensile yield strength	MPa	61.8
Compressive yield strength	MPa	50.6
Tensile ultimate strength	MPa	74

Table 4.7: Polymer material engineering properties

transition from tensile to normal loading at the blade junction.

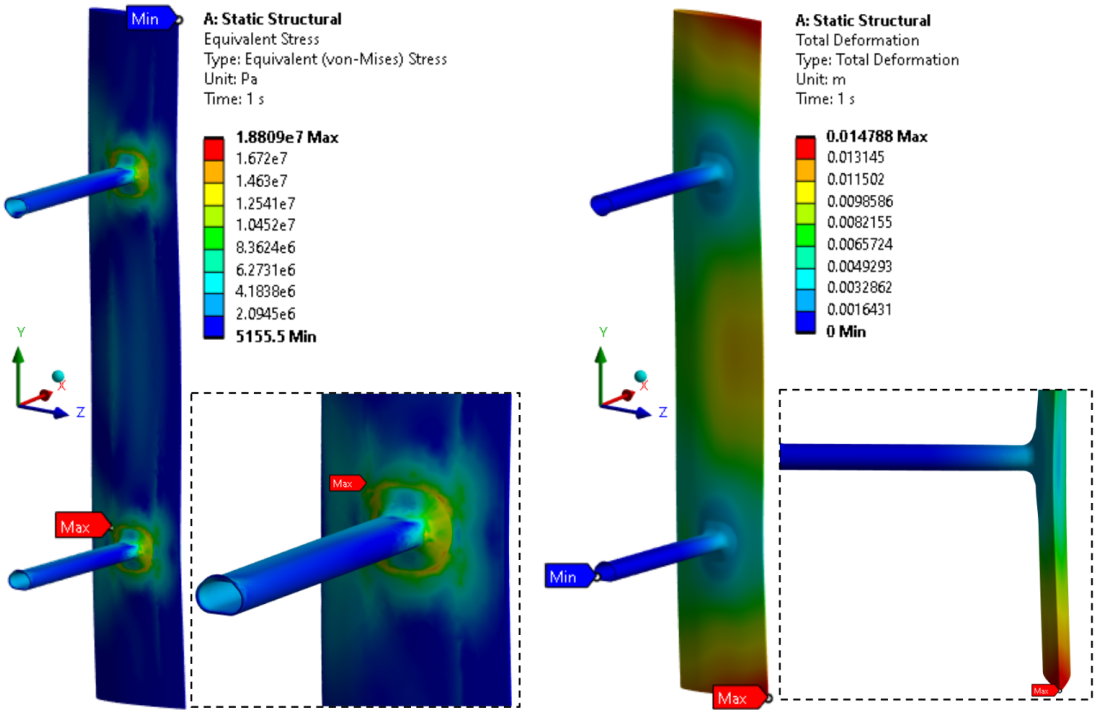

Figure 4.20: Stresses and deformation at maximum wind speed

The most significant deformation occurs at the trailing edges of the blade's extreme ends, due to their lack of support. However, the region along the trailing edge between the two

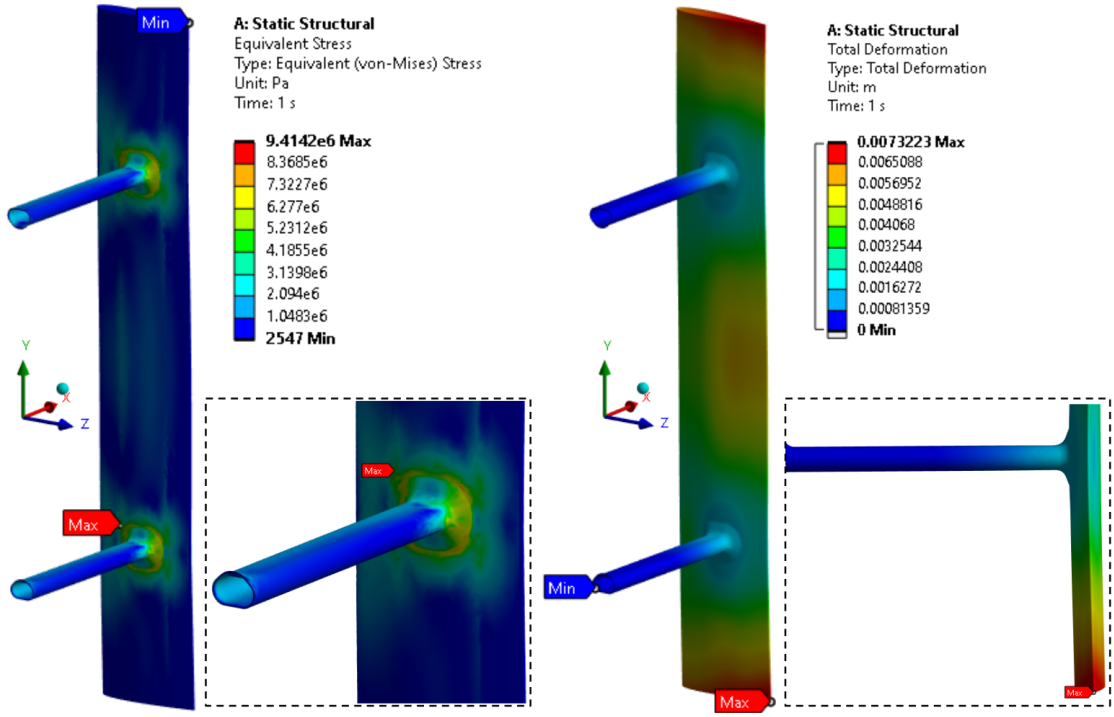

Figure 4.21: Stresses and deformation at average wind speed

struts also experiences sagging as a result of normal loads to a lesser extent compared to the blade ends.

Likewise, in the scenario of maximum wind speed, stress concentration occurs at the junction between the strut and blade, while deformations manifest themselves primarily at the extremities of the blade. These stresses and deformations exhibit greater magnitudes compared to previous conditions, as illustrated in Figure 4.20.

To mitigate the overall deformations observed in this analysis, potential strategies include introducing supplementary support mechanisms such as tension strings extending from the central shaft to the blade, increasing the number of struts, and optimizing the placement.

The Factor of safety represents the margin of safety between the maximum load a structure can withstand and the actual load it experiences during operation. For VAWT blades rotating at high revolutions per minute, ensuring a sufficient factor of safety is essential to prevent catastrophic failures and ensure long-term performance. for safe operations, the fac-

tor of safety must be greater than 1. For extreme wind conditions, the analysis yields an FOS of 2.8 and for average wind conditions, the FOS value is found to be 5.6. This indicates that the designed configuration of the wind turbine blade is capable of withstanding loads in both normal and maximum conditions as shown in Figure 4.22 and carries a minimum safety factor of 2.8 in extreme wind conditions. All three blades are assumed to be identical in masses and design configuration.

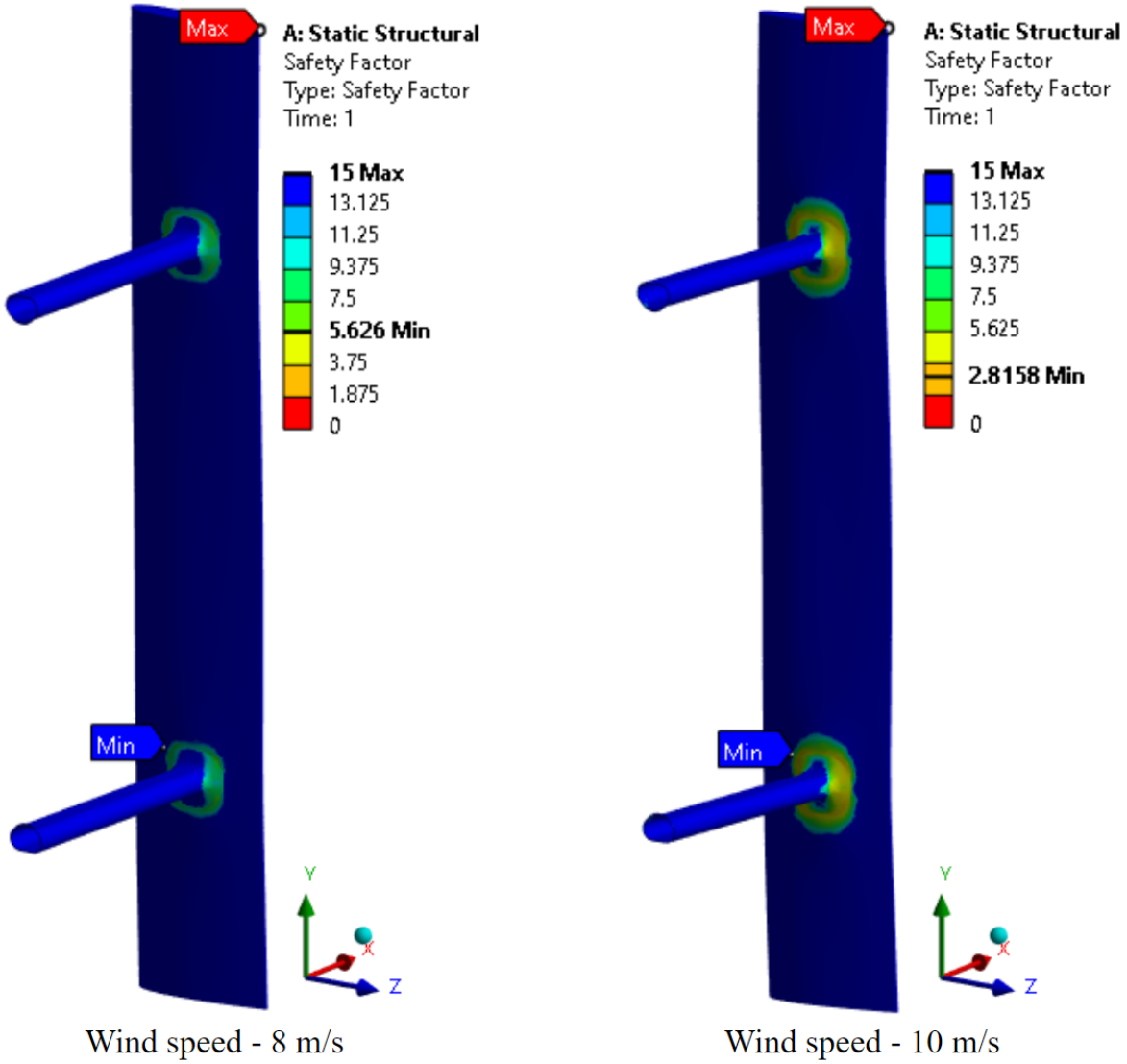

Figure 4.22: Factor of safety and average and maximum wind speeds

CHAPTER 5

CONCLUSION

This work presents a comprehensive investigation into the mechanical recycling of PET polymer, enhanced by infusion of graphene nanoparticles into the polymer matrix, and its direct application in the energy sector in the fabrication of vertical-axis wind turbine rotors. Through experimentation and analysis, significant advancements have been achieved in improving the mechanical properties of recycled PET, particularly in terms of Young's modulus and tensile strength, which tend to degrade with successive recycling processes.

The direct application of this novel material in the construction of VAWT rotors holds immense promise, especially in regions such as East Sudan, where energy crises persist for several reasons. Leveraging the wind energy potential of the region, this work aims to address energy shortages and contribute to sustainable development. By employing computer-aided design modeling, the VAWT rotor was constructed from graphene-reinforced PET, incorporating an internal hollow structure consisting of thin walls and I beams. This structure can achieve a weight class similar to or lighter than aluminum blade turbine rotors. This offers a promising alternative to traditional metal blade rotors.

Aerodynamic analysis of defined turbine configuration gives an exact idea of the forces acting on the turbine rotors while operating at average (8 m/s) and maximum (10 m/s) wind speeds in the chosen region. Furthermore, examination of total loads generated on turbine blades and subsequent analysis of material behavior have demonstrated the ability of the graphene-reinforced PET polymer to withstand operational stresses with a minimum safety factor of 2.8, ensuring safe and reliable turbine operation. This breakthrough not only enhances the viability of recycled polymer VAWT rotor technology but also signifies a significant step towards reducing the environmental impact of renewable energy systems.

The transition from traditional aluminum-based VAWT rotors to graphene-reinforced PET polymer represents a paradigm shift towards sustainability and circular economy principles. Using recycled materials and reducing the carbon footprint associated with rotor production, we can contribute to a greener future while simultaneously fostering the circular economy of polymers.

In essence, this thesis underscores the transformative potential of advanced materials and innovative design concepts in the realm of renewable energy technology. Through interdisciplinary collaboration and a commitment to sustainable practices, we can pave the way for a more resilient and environmentally conscious energy landscape.

BIBLIOGRAPHY

[1] Inc. Whimsical. The iterative workspace for product teams. https://whimsical.com/home, 2024. Accessed: April 24, 2024.

[2] Michael Bozlar, Delong He, Jinbo Bai, Yann Chalopin, Natalio Mingo, and Sebastian Volz. Carbon nanotube microarchitectures for enhanced thermal conduction at ultralow mass fraction in polymer composites. *Advanced materials*, 22(14):1654–1658, 2010.

[3] Vitaliano Dattilo. *CO2 Capture and Sequestration Using Nanomaterials*. PhD thesis, Politecnico di Torino, 2022.

[4] Philip Marsh, Dev Ranmuthugala, Irene Penesis, and Giles Thomas. Numerical simulation of the loading characteristics of straight and helical-bladed vertical axis tidal turbines. *Renewable Energy*, 94:418–428, 2016.

[5] Lahouari Khadir and Hatem Mrad. Numerical investigation of aerodynamic performance of darrieus wind turbine based on the magnus effect. *The International Journal of Multiphysics*, 9(4):383–396, 2015.

[6] Ion Paraschivoiu. *Wind turbine design: with emphasis on Darrieus concept*. Presses inter Polytechnique, 2002.

[7] Sofiane Belmadi and Hichem Kadri. The conflict over resources in sudan between major powers-economic impacts and geopolitical consequences. *Journal of North African Economies*, 20(34):119–136, 2024.

[8] Neil N. Davis, Jake Badger, Andrea N. Hahmann, Brian O. Hansen, Niels G. Mortensen, Mark Kelly, Xiaoli G. Larsén, Bjarke T. Olsen, Rogier Floors, Gil Lizcano, Pau Casso, Oriol Lacave, Albert Bosch, Ides Bauwens, Oliver James Knight,

Albertine Potter van Loon, Rachel Fox, Tigran Parvanyan, Søren Bo Krohn Hansen, Duncan Heathfield, Marko Onninen, and Ray Drummond. The global wind atlas: A high-resolution dataset of climatologies and associated web-based application. *Bulletin of the American Meteorological Society*, 104(8):E1507 – E1525, 2023.

[9] David Marten. Joseph Saverin. Robert Behrens de Luna. Sebastian Perez-Becker. Qblade - next generation wind turbine simulation. https://qblade.org/, 2019. Accessed: April 29, 2024.

[10] Vitaliano Dattilo, Kunal Bachim, Isabella Hague, Brian J. Shonkwiler, Andrew Makeev, Melissa S. Orr, Robin T. Macaluso, and Michael Bozlar. 3d printable flame retardant graphene-polymer nanocomposites. In *Proceedings of the American Society for Composites-thirty-eighth Technical Conference*, 2023.

[11] Mc 5 micro compounders - xplore instruments. https://www.xplore-together.com/products/micro-compounders-mc-5. Accessed: April 29, 2024.

[12] Micro fibre line - xplore instruments. https://www.xplore-together.com/products/micro-fibre-line. Accessed: April 29, 2024.

[13] PTC Onshape. Education plan — onshape product development platform. https://www.onshape.com/en/blog/educational-cad-software-academic-research-innovative-teaching, 2015. Accessed: April 29, 2024.

[14] Huei-Huang Lee. *Finite Element Simulations with ANSYS Workbench 2023: Theory, Applications, Case Studies*. SDC publications, 2023.

[15] The MathWorks Inc. Matlab version: 23.2.0.2485118 (r2023b) update 6, 2023.

[16] Shimadzu Scientific Instruments. Shimadzu ag-x plus. https://www.ssi.shimadzu.com/products/materials-testing/uni-ttm/autograph-ags-x-series/spec.html. Accessed: April 21, 2024.

[17] American Society for Testing and Materials. *Standard Test Method for Tensile Strength and Young's Modulus of Fibers*. ASTM international, 2020.

[18] Oana M Istrate, Keith R Paton, Umar Khan, Arlene O'Neill, Alan P Bell, and Jonathan N Coleman. Reinforcement in melt-processed polymer–graphene composites at extremely low graphene loading level. *Carbon*, 78:243–249, 2014.

[19] Mazharul Islam, David S-K Ting, and Amir Fartaj. Aerodynamic models for darrieus-type straight-bladed vertical axis wind turbines. *Renewable and sustainable energy reviews*, 12(4):1087–1109, 2008.

[20] Mojtaba Ahmadi-Baloutaki, Rupp Carriveau, and David SK Ting. Straight-bladed vertical axis wind turbine rotor design guide based on aerodynamic performance and loading analysis. *Proceedings of the Institution of Mechanical Engineers, Part A: Journal of Power and Energy*, 228(7):742–759, 2014.

[21] Ion Paraschivoiu and Francois Delclaux. Double multiple streamtube model with recent improvements (for predicting aerodynamic loads and performance of darrieus vertical axis wind turbines). *Journal of energy*, 7(3):250–255, 1983.

[22] Karl H Bergey. The lanchester-betz limit (energy conversion efficiency factor for windmills). *Journal of Energy*, 3(6):382–384, 1979.

[23] Faisal Mahmuddin, Syerly Klara, Husni Sitepu, and Surya Hariyanto. Airfoil lift and drag extrapolation with viterna and montgomerie methods. *Energy Procedia*, 105:811–816, 2017.

[24] Travis Justin Carrigan. *Aerodynamic shape optimization of a vertical axis wind turbine*. The University of Texas at Arlington, 2011.